INTRINSIC VISCOSITY AND THE POLARIZABILITY OF PARTICLES HAVING A WIDE RANGE OF SHAPES

J. F. DOUGLAS* AND E. J. GARBOCZI†

Polymers and Building Materials Divisions†*
National Institute of Standards and Technology, Gaithersburg, MD 20899

CONTENTS

The intrinsic viscosity $[\eta]$ and the electric α_e and magnetic α_m polarizabilities of objects having general shape are required in the calculation of some of the most basic properties of solid–solid composites and fluid–solid mixtures. Specifically, the leading order virial coefficients of diverse properties (viscosity, refractive index, dielectric constant, magnetic permeability, thermal and electrical conductivity, and others) can often be expressed in terms of these functionals of object shape. These virial coefficients also provide basic input into effective medium theories describing higher concentration mixtures. The electric and

Advances in Chemical Physics, Volume XCI, Edited by I. Prigogine and Stuart A. Rice.
ISBN 0-471-12002-2

magnetic polarizability tensors have independent interest in applications involving the scattering of electromagnetic and pressure waves from objects of general shape. We present an argument that the ratio of $[\eta]$ and $\langle \alpha_e \rangle$ (the average electric polarizability tensor trace) is an *invariant* to a good approximation. Many analytical and numerical finite element results for a variety of shapes are presented to support the conjectured relation. Our *approximate* relation between $[\eta]$ and $\langle \alpha_e \rangle$ complements the *exact* relation between the hydrodynamic virtual mass **W** and the magnetic polarizability $\boldsymbol{\alpha}_m$ tensors.

I. INTRODUCTION

There are numerous contributions to the problem of predicting the effective properties of inhomogeneous materials [1–3] and reviews appear regularly on this topic. Here we focus the discussion on transport properties [1], such as the viscosity of suspensions, dielectric constant, refractive index, thermal conductivity, and related physical properties of mixtures. Much of the research has been limited to the classical case of spherical particle suspensions and composites and a few other particle shapes that allow analytical treatment [4–20]. Even for suspensions of hard spheres in fluids, rigorous results are limited to the first couple of virial coefficients [4–20] and analytical bounds on the effective properties at higher volume fractions [21, 22]. Recent progress has been made in the numerical calculation of transport properties by finite element [23] and Brownian dynamics methods [24], which is associated with the advent of sufficiently powerful computational resources and faster computational algorithms such as the conjugate gradient method [25]. These new numerical results are very helpful in testing theoretical ideas about the effective properties of mixtures.

Much of the previous research, even the more recent numerical work, has focused on mixtures involving simple shapes, such as spheres, since the overall goal has usually been the development of a theory applicable at high volume fractions of suspended matter. The choice of simple particle shapes is motivated by the existence of the relatively few exact analytical results at lower concentrations, which provide a benchmark test for the numerical calculations.

However, many real particles in fluid–solid suspensions and in solid composites are not well represented by these simple shapes. The present work allows for general centrosymmetric particle shape, while focusing solely on the dilute limit. This is a natural first step towards treating complex-shaped particle mixtures at higher concentrations. Originally, the research was motivated by theoretical arguments, described below,

that suggested a relation between the leading order virial coefficients for the viscosity and conductivity of suspensions of conducting particles having *arbitrary* shape. We have gathered analytical results for these properties, which are scattered widely throughout the mathematical and technical literature and have calculated new results as necessary (analytically and by finite element methods) to obtain a wide range of shapes with which to check the conjectured relation. The results obtained should have independent interest in the problem of developing a more realistic description of the properties of mixtures in terms of a more faithful description of the mixture components.

In Section II we summarize classical results for the conductivity virial expansion and discuss the relation between the leading virial coefficient, called the intrinsic conductivity $[\sigma]$ and certain functionals of particle shape that arise in other physical contexts—the electric polarizability, magnetic polarizability, and virtual mass. All these functionals of shape involve solving the Navier–Stokes or the Laplace equations on the exterior of a body with various boundary conditions [26, 27]. Exact results for these functionals are summarized for simple particle shapes to illustrate the general effect of particle anisotropy.

Section III summarizes classical results for the viscosity virial expansion of suspensions of particles and the virial expansion for the shear modulus of an elastic material with inclusions. An angular preaveraging approximation is invoked, as in previous calculations for the translational friction of a Brownian particle [27], to relate the intrinsic viscosity $[\eta]$ to the intrinsic conductivity $[\sigma]_\infty$ for highly conducting inclusions. The intrinsic viscosity is the leading order virial coefficient for the viscosity of a dilute mixture. Examination of exact results for $[\eta]$ and $[\sigma]_\infty$ show that the conjectured relation is not exact, but is a rather good approximation. An extensive range of particle shapes is considered in this comparison. In Section IV we pursue the universality of the $[\eta]-[\sigma]_\infty$ relation for a variety of complicated shapes using finite element methods. The conjectured relation between $[\eta]$ and $[\sigma]_\infty$ is found to hold to a good approximation ($\pm 5\%$) for all shapes considered.

More general results are possible in $d=2$ due to general conformal mapping methods. We exploit a mathematical identity of Pólya [26, 28], which implies that $[\sigma]$ for conducting and nonconducting inclusions is *exactly* related to the "transfinite diameter" C_L of the inclusions. This relation is useful since this quantity is fundamental in classical conformal mapping theory and, consequently, this property has been extensively investigated [26, 29, 30]. All previously known exact results for $[\sigma]_\infty$ in $d=2$, plus many new results, are obtained from our new relation expressing $[\sigma]_\infty$ purely in terms of the *geometrical* quantities, C_L and the

particle area. Numerical results for $[\eta]$ in $d = 2$ are obtained using finite element methods. Again the predicted approximate relation between $[\eta]$ and $[\sigma]_\infty$ is well confirmed. Analytical results for ellipses show that the conjectured relation is actually *exact* at all aspect ratios and we conjecture that $[\eta]$ equals $[\sigma]_\infty$ for all shapes in two dimensions.

Section VI considers the case of flat "plate-like" objects, which requires special analytic treatment. Plate-like particles are intermediate in their properties between the three- and two-dimensional (3D and 2D) cases and these problems tend to be especially difficult analytically. Numerical finite element calculations, however, can be carried out using methods similar to those used for other shapes (see Appendix E). This case has important applications in the scattering of sound waves and electromagnetic radiation through apertures and many numerical results have accumulated in the technical literature. We summarize these connections since they provide the source of predictions for $[\eta]$ through our proposed relation between $[\eta]$ and $[\sigma]_\infty$.

II. POLARIZABILITY, INTRINSIC CONDUCTIVITY, AND VIRTUAL MASS

Maxwell [4a] first considered the classic problem of the conductivity σ of a particle suspension in which the suspended particles have a different conductivity σ_p than the suspending medium σ_0. He recognized that the change in conductivity reflected the average dipole moment induced by the particles on the suspending medium in response to an applied field. For a dilute suspension of hard spheres the effect is the simple additive sum of the effects caused by the individual particle dipoles. The effective conductivity σ of the dilute mixture then equals,

$$\sigma/\sigma_0 = 1 + [3(\Delta_\sigma - 1)/(\Delta_\sigma + 2)]\phi + O(\phi^2), \qquad \Delta_\sigma \equiv \sigma_p/\sigma_0 \quad (2.1a)$$

where Δ_σ is the "relative conductivity" and ϕ is the volume fraction of suspended particles. Exact results that go beyond this classic result are limited, however. There are effective medium calculations [3] that attempt to extend the "virial expansion" [Eq. (2.1a)] to higher powers of ϕ. Sangani [5] recently generalized Maxwell's calculation for spherical particles to d dimensions. The second virial coefficient for σ/σ_0 was calculated by Levine and McQuarrie [6] for conducting spheres ($\Delta_\sigma \to \infty$), while Jefferey [7] treated the case of arbitrary Δ_σ.

The virial expansion [Eq. (2.1a)] has been verified experimentally for dilute suspensions of numerous substances. For example, the leading order virial coefficient for conducting spheres equals 3. This value has

been observed by Voet for nearly spherical iron particles (diameter = 10 μm) in linseed and mineral oils [31]. Emulsions of salt water in fuel oil and mercury drops in different oils have also been found to be consistent with Eq. (2.1a) where Δ_σ is large [32]. The corresponding prediction for insulating suspended spheres (Δ_σ near 0) has been observed for suspensions of glass beads and sand particles in salt solutions [33] and for gas bubbles in salt solutions [34]. The virial coefficient notably changes sign and equals $-\frac{3}{2}$ in the insulating spherical particle suspension. Good agreement with Eq. (2.1a) has also been observed in fluidized beds where Δ_σ was tuned over a range of values [35].

At higher concentrations the independent particle approximation of the dilute regime no longer holds, but the leading order virial coefficient still plays a primary role in theoretical estimates of the high concentration variation of transport properties. In the simple effective medium theories of Bruggeman [36] and Brinkman [37], for example, the resummation of the virial expansion for an arbitrary transport property P of a suspension is quite generally given by,

$$P/P_0 \approx (1-\phi)^m \tag{2.1b}$$

where P_0 is the property for a pure suspending medium. Consistency at low concentration requires that the "critical exponent" m has the same magnitude as the leading order virial coefficient. This simple prediction, which is derived on the basis of very simplistic reasoning, is often in remarkably good agreement with observations in physically important systems [31–33,38–41]. For example, Archie's law for the conductivity of rocks saturated with salt water [39, 41] follows directly from Eqs. (2.1a) and (2.1b). The corresponding Brinkman–Roscoe [37, 38] result has also been cited often as a useful description of the viscosity of concentrated suspensions. We mention these approximate calculations only to illustrate the primary role of the leading order virial coefficient in developing a theoretical description of mixture properties at higher concentrations. The following development is restricted to the low concentration regime, where such uncontrolled approximations are unnecessary.

The practically important inverse problem of determining the volume fraction of a suspension of complicated shaped particles from electrical measurements motivated the generalization of Eq. (2.1a) to particles having arbitrary shape. Fricke [8] treated the case of ellipsoidal particles and utilized a Clausius–Mosotti style [42] effective medium theory to approximate the higher concentration regime. These effective medium calculations are exact in the dilute regime where they reduce to a virial expansion of the form for Eq. (2.1a).

The low concentration σ virial expansion of randomly oriented and arbitrarily shaped particles equals [43, 44]:

$$\sigma/\sigma_0 = 1 + [\sigma]\phi + O(\phi^2) \tag{2.2a}$$

$$[\sigma] \equiv \lim_{\phi \to 0^+} (\sigma - \sigma_0)/(\sigma_0 \phi) \tag{2.2b}$$

where $[\sigma]$ is the "intrinsic conductivity." The magnitude of $[\sigma]$ can be rapidly varying for extended or flat particles depending on the relative conductivity Δ_σ, so that the effect of adding a given amount of material to a suspension can be greatly dependent on particle shape and composition. It is often convenient to define virials such as $[\sigma]$ in terms of a number concentration when the suspended particles have zero volume, as in the cases of needles, plates, and idealized random walk chains, for example.

The "polarizability" $\boldsymbol{\alpha}$ describes the average dipole moment induced on a particle in an applied field (electric or magnetic) and the calculation of the virial coefficient $[\sigma]$ therefore requires the determination of $\boldsymbol{\alpha}$ or at least an average of the matrix elements defining $\boldsymbol{\alpha}$ (see below). The quantity $\boldsymbol{\alpha}$ is a second rank tensor [4b,44] that depends on particle orientation, shape, size, and the ratio of the particle property to the matrix property for the property that is being considered [see Eqs. (2.1a) and (2.5b)]. The average polarizability $\langle \alpha \rangle$, which is $1/d$ times the trace of the polarizability tensor, is a scalar that is invariant under particle rotations [45, 46]. The polarizability has the units of volume so that the ratio of $\langle \alpha \rangle$ and the particle volume V_p is a scale invariant functional of particle shape and Δ_σ. Calculation of $\langle \alpha \rangle$ is often easier than the full polarizability tensor $\boldsymbol{\alpha}$, since any three orthogonal directions can be chosen for the field directions in the calculation of $\langle \alpha \rangle$. Equivalently, we can angularly average $\boldsymbol{\alpha}$ over all orientation angles with uniform probability [45, 46] to obtain $\langle \alpha \rangle$. In some applications it is useful to orient the suspended particles, in which case the effective conductivity $\boldsymbol{\sigma}$ of the composite becomes explicitly dependent on $\boldsymbol{\alpha}$ [9]. Historically, the anisotropic case was found to be important in the design of microwave lenses and other artificial dielectrics where large scale conducting elements are arrayed in an insulating matrix [47–50]. The anisotropic situation is also encountered in the optical properties of sheared anisotropic particle suspensions [51]. In this chapter, we emphasize the average polarizability $\langle \alpha \rangle$, which is relevant to suspensions in which the particle orientation is completely random.

In an electrostatic context the polarizability describes how the charges of a body of dielectric constant ε_p, embedded in a medium having a dielectric constant ε_0, are distorted in response to an applied electric field

[42, 52]. The distorted charge distribution gives rise to a dipolar field that reacts upon the applied field, thereby modifying the net effective field in the proximity of the body. This connection between conductivity and the dielectric constant is natural since Eqs. (2.1) and (2.2) also describe the dielectric constant of suspensions of particles with a relative dielectric constant $\Delta_\varepsilon = \varepsilon_p/\varepsilon_0$. Moreover, these equations apply equally well to the magnetic permeability, diffusion coefficient (see Appendix A), and the thermal conductivity of dilute suspensions, where the magnetic field, concentration gradient, and the temperature gradient are the corresponding "fields" [1, 2, 21d].

Although simple in principle, the calculation of the polarizability tensor for objects of general shape is a mathematical problem of notorious difficulty. Indeed, the ellipsoid [8, 52] is the only shape for which exact analytic results have been obtained as a function of Δ_σ. There have been recent numerical calculations of the polarizability tensor for other objects in relation to Rayleigh scattering (e.g., radar) applications [53, 54]. The situation is better for limiting values of the relative conductivity Δ_σ where the polarizability tensor $\boldsymbol{\alpha}(\Delta_\sigma)$ simplifies. For highly conducting (superconducting) inclusions, the polarizability tensor reduces to the electric polarizability $\boldsymbol{\alpha}_e$,

$$\lim_{\Delta_\sigma \to \infty} \boldsymbol{\alpha}(\Delta_\sigma) \equiv \boldsymbol{\alpha}_e \tag{2.3a}$$

and $[\sigma]$ for randomly oriented inclusions, having a much higher conductivity than the matrix, equals,

$$[\sigma(\Delta_\sigma \to \infty)] \equiv [\sigma]_\infty = \langle \alpha_e \rangle / V_p \tag{2.3b}$$

where $\langle \boldsymbol{\alpha}_e \rangle$ denotes the average electric polarizability tensor. The case of insulating inclusions in a conducting medium corresponds formally to $\Delta_\sigma \to 0^+$, so that we have

$$\lim_{\Delta_\sigma \to 0} \boldsymbol{\alpha}(\Delta_\sigma) \equiv \boldsymbol{\alpha}_m \tag{2.4a}$$

$$[\sigma(\Delta_\sigma \to 0^+)] \equiv [\sigma]_0 = \langle \alpha_m \rangle / V_p \tag{2.4b}$$

where $\boldsymbol{\alpha}_m$ is the magnetic polarizability with $\langle \alpha_m \rangle$ as the corresponding average. In the $\Delta_\sigma \to 0^+$ and $\Delta_\sigma \to \infty$ limits $[\sigma]$ is simply a functional of particle shape and spatial dimension. Many specific examples are given below. We note that $[\sigma]$ is rather insensitive to particle shape when the conductivity of the particles is similar to the embedding medium ($\Delta_\sigma \approx 1$). In this limit $[\sigma]$ equals [42b],

$$[\sigma] = (\Delta_\sigma - 1) + O[(\Delta_\sigma - 1)^2] \tag{2.4c}$$

which is completely independent of particle shape in leading order.

The limiting relations [Eqs. (2.3b) and (2.4b)], connecting the intrinsic conductivity to the electric and magnetic polarizabilities of a conductor, can be appreciated from a more general relation between the generalized electric **E** and magnetic **H** field polarizability tensors, $\boldsymbol{\alpha}(\mathbf{E})$ and $\boldsymbol{\alpha}(\mathbf{H})$, which allows a unified discussion of the response of complicated shaped objects to both electrostatic and magnetostatic fields. Senior [55] has proven the validity of the general relations,

$$\boldsymbol{\alpha}(\mathbf{E}) = \mathbf{X}(\Delta_\varepsilon), \qquad \boldsymbol{\alpha}(\mathbf{H}) = -\mathbf{X}(\Delta_\mu) \tag{2.5a}$$

where Δ_ε and Δ_μ are the relative dielectric constant and magnetic permeability,

$$\Delta_\varepsilon = \varepsilon_p/\varepsilon_0, \qquad \Delta_\mu = \mu_p/\mu_0 \tag{2.5b}$$

and **X** is the *same* function for *both* electric and magnetic fields. A perfect conductor ($\Delta_\varepsilon \to \infty$) is "magnetically impermeable" ($\Delta_\mu \to 0^+$), while a perfect insulator (($\Delta_\varepsilon \to 0^+$) is formally a "magnetic conductor" ($\Delta_\mu \to \infty$) [50, 56]. The relevance of the magnetic polarizability in describing the insulating limit ($\Delta_\varepsilon \to 0^+$) of the intrinsic conductivity is thus apparent.

Keller et al. [57] recently emphasized the *equivalence* of the magnetic polarizability tensor $\boldsymbol{\alpha}_m$ and the hydrodynamic effective mass tensor **M** describing a particle translating through an inviscid, irrotational, and incompressible ("perfect") liquid. The parameter **M** is equal to the particle volume V_p plus the "added mass" or "virtual mass" **W** associated with the kinetic energy imparted to the fluid from the particle motion,

$$\boldsymbol{\alpha}_m = -\mathbf{M}, \qquad \mathbf{M} = V_p\mathbf{I} + \mathbf{W} \tag{2.6}$$

where **I** is the identity matrix. The minus sign indicates that each matrix element is multiplied by -1. (Sometimes these tensors $\boldsymbol{\alpha}_m$ and **M** are defined to have the same sign.) The fundamental relation Eq. (2.6) was indicated earlier by Kelvin [58] and implicitly by others [59].

Almost all hydrodynamic calculations of **M** assume that the particle density is much higher than the surrounding fluid. Birkhoff and co-workers [60–63] showed that the dipolar field disturbance induced by the motion of particles having comparable density to the fluid medium involve the general polarizability tensor **X** in Eq. (2.5a), where the field permittivity parameter corresponding to Δ_σ is related to the relative density of the particle and the fluid. This generalized relation implies that

M of low density objects (e.g., air bubbles in water) corresponds to $\boldsymbol{\alpha}_e$ rather than $\boldsymbol{\alpha}_m$ [60]. In the following discussion we restrict ourselves to the more conventional case in which the moving object is assumed to have a much higher density than the fluid. The terms effective mass and virtual mass will then always imply the Keller–Kelvin relation [Eq. (2.6)]. A *nonperturbative* generalization of Eq. (2.6) to finite concentrations is discussed in Appendix A.

It should be mentioned that the hydrodynamic applications of **M** are not limited to transient hydrodynamic phenomena associated with the forces on accelerating particles in a fluid medium [64,65]. The presence of a body in a converging stream of an inviscid fluid, such as air in a wind tunnel impinging on an aircraft model, gives rise to a force on the body that is determined by the **M** tensor [**M** equals $(3V_p/2)\mathbf{I}$ for a sphere and the angular average of **M** for near-spherical and slender particles usually differs little from the sphere value; see below] and the pressure gradient in the channel. The force is in the direction of the pressure gradient. Thomson (Lord Kelvin) [66] and Taylor [67] showed that this "buoyancy drag force" is obtained even in non-simply connected spaces, like porous media. The Kelvin–Taylor result for drag forces in "perfect" fluids is a natural counterpart to the Stokes drag force [64] on slowly translating particles in viscous fluids, where a shape functional similar to **M** arises [see Eq. (3.10)].

The importance of Eqs. (2.3b), (2.4b), and (2.6) derives from the extensive mathematical and technical literature relating to the calculation of $\boldsymbol{\alpha}_e$ and **M** [6, 26, 46, 52, 68–76]. These functionals of object shape are naturally encountered in the solution of the Laplace equation on the exterior of regions of various shapes. Consequently, these shape functionals have attracted a mathematical interest quite apart from technical applications [26, 46]. For example, it has rigorously been shown that $\langle \alpha_e \rangle$ and $\langle M \rangle$ achieve their *absolute minima* for a circle and sphere in $d = 2,3$ dimensions [26, 77] of all objects having a finite area or volume, respectively. (Presumably, a hypersphere minimizes these functionals in d dimensions, $d \geq 2$.) Numerical illustrations of this sphere minimization property are presented below. It is also known (implicitly from the work of Keller and Mendelson [78]) that $\langle \alpha_e \rangle = -\langle \alpha_m \rangle$ in $d = 2$ and that these shape functionals have a general geometric interpretation in terms of conformal mapping, as will be discussed in Section V below.

Payne and Weinstein [79] proved that some components of $\boldsymbol{\alpha}_e$ and **M** for certain regions (having reflection symmetry in $d = 2$ or axisymmetric particles in $d = 3$) are related to the capacity C of the region. The capacity C is another shape functional related to solving the Laplace equation on the exterior of a particle. Numerous applications of this

quantity are summarized in [80], which also describes a probabilistic method for calculating C by hitting a region of arbitrary shape with Brownian paths launched from an enclosing surface. This development makes the Payne–Weinstein relation attractive for the calculation of $\boldsymbol{\alpha}_e$ and $\boldsymbol{\alpha}_m$.

Finally, we mention that exact calculations of $\boldsymbol{\alpha}_e$ and $\mathbf{M}$ can be made for certain object boundaries and associated coordinate systems for which the Laplace equation is separable [46] and for regions related to the separable boundary cases by Kelvin inversion [4, 52b]. This leads to quite a few intrinsic conductivity results for objects with interesting shapes that are useful in checking numerical methods applicable to more generally shaped regions. Some results of this kind are summarized below.

The technology literature is also a rich source of results for $\boldsymbol{\alpha}_e$, $\boldsymbol{\alpha}_m$, and $\mathbf{M}$. Apart from the relation to transport coefficients like σ, ε, μ, and D, mentioned above, the magnetic and electric polarization tensors have fundamental interest because they *completely determine* [55–57] the scattering of electromagnetic waves having long wavelengths relative to the (metallic) scattering object size, this is, Rayleigh scattering [81]. It is a crucial application to discriminate object shape to the maximum extent possible from long wavelength radiation like radar and, needless to say, the technical literature reflects a preoccupation with objects having the shapes of missiles and space vehicles [53, 68]. Weather radar applications are also important [82]. We also note that scattering of long wavelength sound waves from hard obstacles is determined by $\mathbf{M}$ and the particle volume V_p [83–86] and that $\boldsymbol{\alpha}_e$ and $\mathbf{M}$ are also fundamental in the scattering of electromagnetic and sound waves through apertures [72, 87–91]. These applications especially require the calculation of $\boldsymbol{\alpha}_e$ and $\mathbf{M}$ for plate-shaped objects [92].

Next, we tabulate the components of the polarization tensors $\boldsymbol{\alpha}_e$ and $\boldsymbol{\alpha}_m$ for ellipsoids, since this information is important in the comparisons below with intrinsic viscosity data. These tabulations should give the reader some feeling for the magnitudes involved and illustrate some of the general ideas stated above.

The ellipsoid provides the simplest example of an object having variable shape. Appendix B summarizes the necessary mathematical and numerical computations involved in calculating $\boldsymbol{\alpha}_e$ (ellipsoid) for a range of principal axis radii ratios. In Figs. 2.1 and 2.2 we present the polarizability results for ellipsoids of revolution per unit particle volume (which actually have closed-form analytical solutions, see Appendix B). Enough points have been calculated to make the graphs of these quantities appear as smooth curves. The abscissa x denotes the length of the ellipsoid along the symmetry direction relative to the axis length

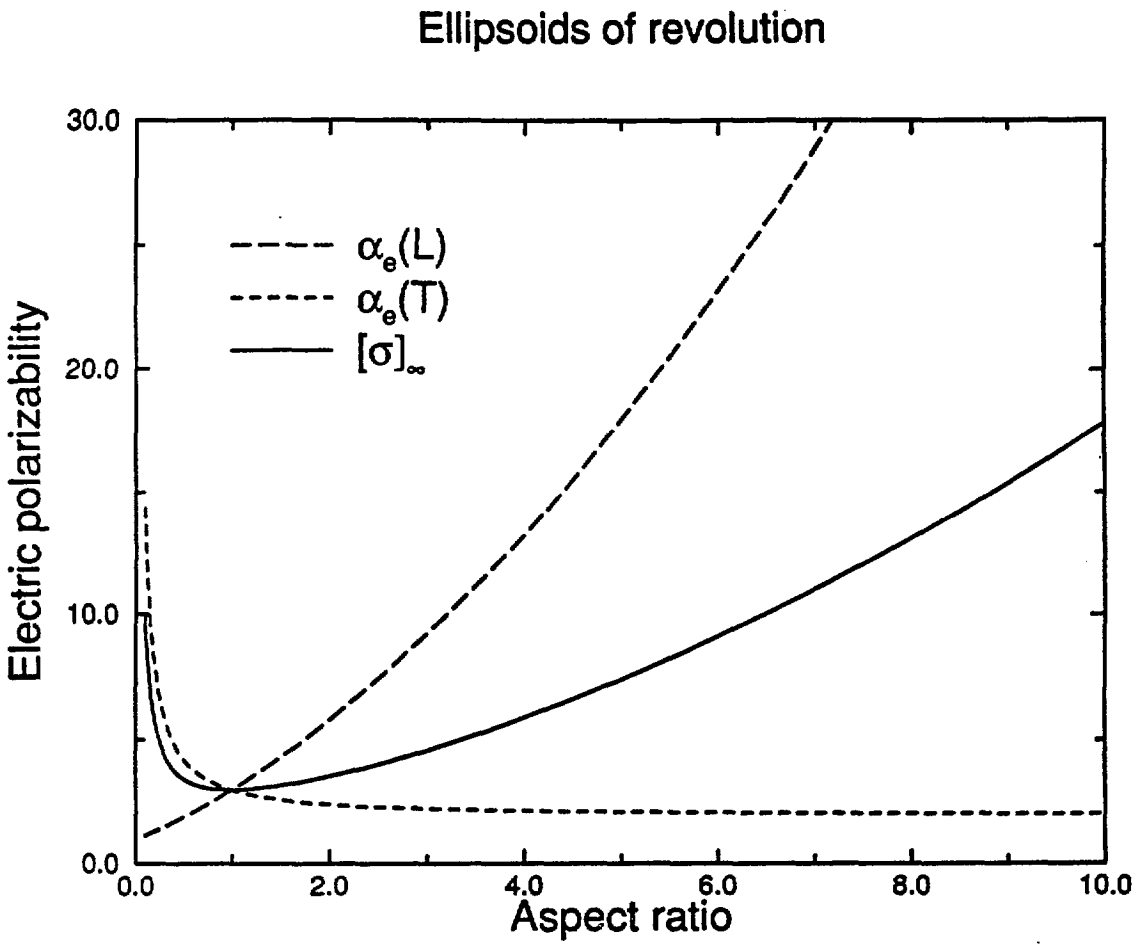

Figure 2.1. The longitudinal (L) and transverse (T) components of the dimensionless (normalized by the particle volume) electric polarizability tensor $\boldsymbol{\alpha}_e$ for ellipsoids of revolution and the average of these components, the intrinsic conductivity of a conductor $[\sigma]_\infty$.

normal to the symmetry axis (aspect ratio). The component of $\boldsymbol{\alpha}_e$ and $\boldsymbol{\alpha}_m$ along the symmetry axis is denoted by L and the component normal to the symmetry axis is denoted by T. The average polarizabilities, $\langle \boldsymbol{\alpha}_e \rangle / V_p = [\sigma]_\infty$ and $\langle \alpha_m \rangle / V_p = [\sigma]_0$, are also shown. These quantities are invariant under particle rotations and are functionals of particle shape only. A tabulation of this numerical data for ellipsoids of revolution is given in Table I. We give the data in the table in the dimensionless form $\boldsymbol{\alpha}/V_p$, since the results are then independent of the absolute particle size. A more general tabulation for the triaxial case is given separately for $\boldsymbol{\alpha}_e$ and $\boldsymbol{\alpha}_m$ in Tables II and III for a range of the two principal axis ratios. All reported digits shown in Tables I–III are significant.

We observe in Figs. 2.1 and 2.2 that the averages $\langle \alpha_e \rangle / V_p = [\sigma]_\infty$ and $\langle \alpha_m \rangle / V_p = [\sigma]_0$ obtain absolute minima for $x = 1$. This accords with the exact results [26, 77] mentioned above, which indicate that this minimum

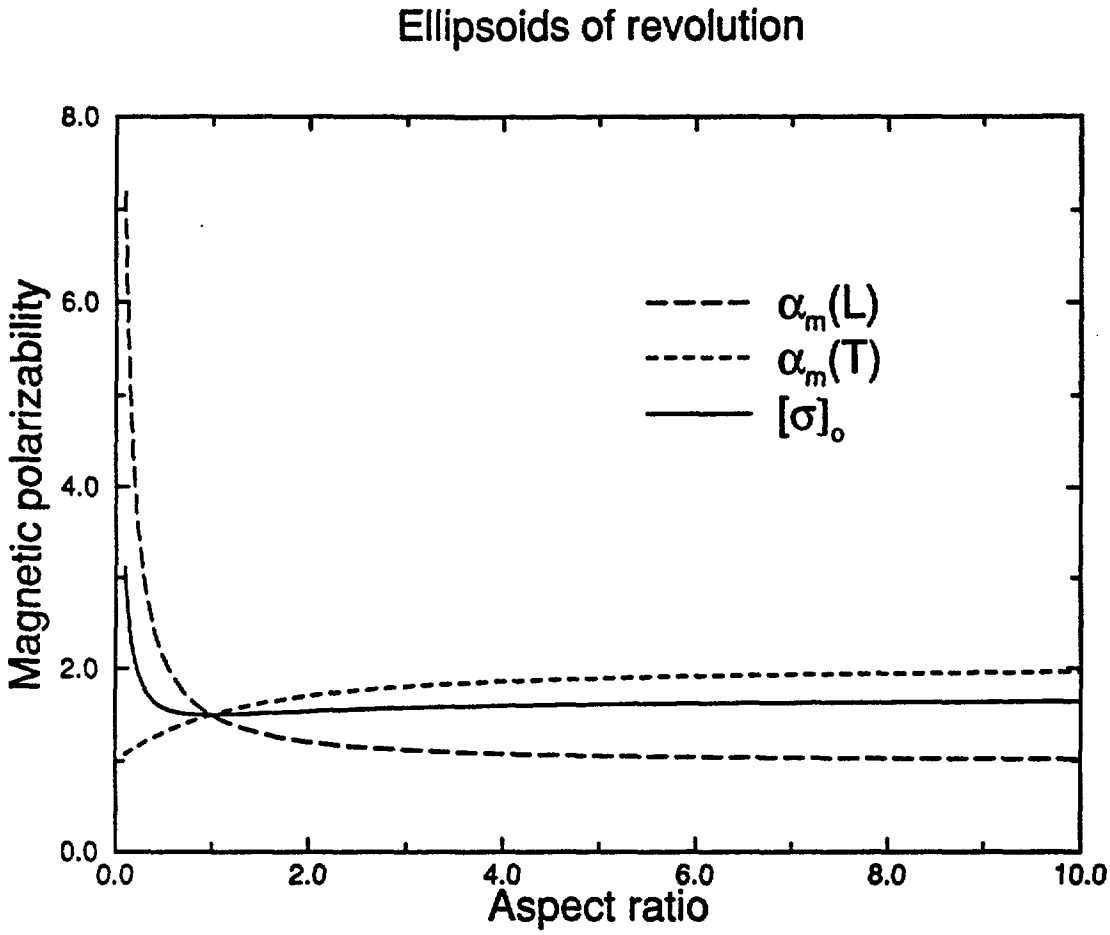

Figure 2.2. The longitudinal (L) and transverse (T) components of the dimensionless (normalized by the particle volume) magnetic polarizability tensor α_m for ellipsoids of revolution and the average of these components, the intrinsic conductivity of an insulator $[\sigma]_0$.

is achieved in the case of a sphere for all objects having a given finite volume. These virial coefficients are observed to be quite sensitive to the aspect ratio x in the approach to the disk limit, but there are also significant effects of particle asymmetry on the virial coefficients for highly *conducting* needlelike ($x \gg 1$) particles. Needlelike *non-conducting* inclusions lead to remarkably little change in the intrinsic conductivity. Thus, we can understand the general experimental observation that nonconducting asymmetric inclusions in a conducting medium often lead to nearly the same intrinsic conductivity [93], except in the case of platelet shaped particles [94]. This implies that the most economical means of making a medium more insulating is through the introduction of a small concentration of nonconducting plate-like particles. Figure 2.2 also suggests that the polarizability of very irregular nonconducting objects, such as alkane chains and other nonconducting polymers, should

TABLE I

Polarizability Components for Ellipsoids of Revolution, Electric and Magnetic (α_e,α_m).

Aspect Ratio	Prolate					
	α_e (L)V_p	α_e(T)/V_p	$[\sigma]_\infty$	α_m(L)/V_p	α_m(T)/V_p	$[\sigma]_0$
2	5.7616	2.4200	3.5339	1.2100	1.7042	1.5395
3	9.1988	2.2439	4.5622	1.1220	1.8039	1.5766
4	13.2613	2.1631	5.8625	1.0816	1.8598	1.6004
5	17.9144	2.1182	7.3836	1.0591	1.8943	1.6159
6	23.1323	2.0904	9.1043	1.0452	1.9171	1.6265
7	28.8946	2.0717	11.0127	1.0358	1.9331	1.6340
8	35.1848	2.0585	13.1006	1.0293	1.9447	1.6396
9	41.9890	2.0488	15.3622	1.0244	1.9535	1.6438
10	49.2954	2.0414	17.7927	1.0207	1.9602	1.6471
20	148.168	2.0136	50.7320	1.0068	1.9866	1.6600
30	290.342	2.0069	98.1188	1.0035	1.9931	1.6632
40	472.623	2.0042	158.877	1.0021	1.9958	1.6646
50	693.013	2.0029	232.339	1.0014	1.9971	1.6652
60	950.083	2.0021	318.029	1.0011	1.9979	1.6656
70	1,242.74	2.0016	415.581	1.0008	1.9984	1.6659
80	1,570.10	2.0013	524.701	1.0006	1.9987	1.6660
90	1,931.43	2.0010	645.147	1.0005	1.9990	1.6661
100	2,326.12	2.0009	776.710	1.0004	1.9991	1.6662
200	8,013.36	2.0002	2,672.45	1.0001	1.9998	1.6665
300	16,675.8	2.0001	5,559.95	1.0001	1.9999	1.6666
400	28,145.8	2.0001	9,383.29	1.0000	1.9999	1.6666
500	42,316.9	2.0000	14,106.9	1.0000	2.0000	1.6666
600	59,112.3	2.0000	19,705.4	1.0000	2.0000	1.6666
700	78,472.2	2.0000	26,158.7	1.0000	2.0000	1.6667
800	100,348.0	2.0000	33,450.8	1.0000	2.0000	1.6667
900	124,700.0	2.0000	41,568.2	1.0000	2.0000	1.6667
1000	151,494.0	2.0000	50,499.4	1.0000	2.0000	1.6667
Reciprocal Aspect Ratio	Oblate					
	α_e(L)/V_p	α_e(T)/V_p	$[\sigma]_\infty$	α_m(L)/V_p	α_m(T)/V_p	$[\sigma]_0$
2	1.8968	4.2301	3.4524	2.1151	1.3096	1.5781
3	1.5738	5.4853	4.1815	2.7426	1.2230	1.7295
4	1.4212	6.7486	4.9728	3.3743	1.1740	1.9074
5	1.3325	8.0155	5.7878	4.0078	1.1425	2.0976
6	1.2746	9.2844	6.6145	4.6422	1.1207	2.2945
7	1.2338	10.5544	7.4476	5.2772	1.1047	2.4955
8	1.2036	11.8253	8.2847	5.9126	1.0924	2.6991
9	1.1802	13.0966	9.1245	6.5483	1.0827	2.9045
10	1.1617	14.3683	9.9661	7.1841	1.0748	3.1112
20	1.0797	27.0935	18.4222	13.5467	1.0383	5.2078
30	1.0529	39.8234	26.8999	19.9117	1.0258	7.3211
40	1.0396	52.5545	35.3829	26.2773	1.0194	9.4387
50	1.0316	65.2862	43.8680	32.6431	1.0156	11.5581
60	1.0263	78.0181	52.3541	39.0090	1.0130	13.6783
70	1.0225	90.7501	60.8409	45.3750	1.0111	15.7991
80	1.0197	103.482	69.3280	51.7411	1.0098	17.9202
90	1.0175	116.214	77.8154	58.1072	1.0087	20.0415
100	1.0158	128.946	86.3030	64.4733	1.0078	22.1630
200	1.0079	256.269	171.182	128.134	1.0039	43.3809
300	1.0052	383.593	256.064	191.796	1.0026	64.6007
400	1.0039	510.917	340.946	255.458	1.0020	85.8209
500	1.0031	638.241	425.828	319.120	1.0016	107.041
600	1.0026	765.565	510.711	382.782	1.0013	128.261
700	1.0022	892.889	595.593	446.444	1.0011	149.482
800	1.0020	1,020.21	680.476	510.106	1.0010	170.702
900	1.0017	1,147.53	765.358	573.768	1.0009	191.923
1000	1.0016	1,274.86	850.241	637.430	1.0008	213.144

TABLE II
Components of the Electric Polarizability Tensor α_e for Triaxial Ellipsoids

a_1	a_2	a_3	$\alpha_e(11)/V_p$	$\alpha_e(22)/V_p$	$\alpha_e(33)/V_p$	$[\sigma]_\infty$
1	2	3	1.7345	3.7432	6.3979	3.9585
1	2	4	1.6587	3.5115	8.9007	4.6903
1	2	5	1.6162	3.3791	11.721	5.5723
1	2	6	1.5894	3.2950	14.847	6.5774
1	2	7	1.5714	3.2375	18.268	7.6924
1	2	8	1.5586	3.1962	21.974	8.9098
1	2	9	1.5490	3.1654	25.959	10.224
1	2	10	1.5418	3.1417	30.215	11.633
1	2	20	1.5140	3.0490	86.743	30.435
1	2	50	1.5030	3.0110	390.06	131.52
1	2	100	1.5009	3.0034	1,283.9	429.47
1	2	300	1.5001	3.0005	9,015.0	3006.5
1	2	500	1.5001	3.0002	22,717.0	7574.0
1	2	1,000	1.5000	3.0001	80,706.0	26903.0
1	3	4	1.4979	5.0419	7.4586	4.6662
1	3	5	1.4548	4.7842	9.6534	5.2975
1	3	6	1.4275	4.6178	12.061	6.0356
1	3	7	1.4089	4.5027	14.676	6.8626
1	3	8	1.3956	4.4190	17.491	7.7688
1	3	9	1.3857	4.3560	20.503	8.7483
1	3	10	1.3781	4.3070	23.706	9.7970
1	3	20	1.3486	4.1107	65.575	23.678
1	3	50	1.3367	4.0258	285.32	96.894
1	3	100	1.3344	4.0081	923.91	309.75
1	3	300	1.3335	4.0012	6,377.3	2127.5
1	3	500	1.3334	4.0005	15,980.0	5328.5
1	3	1,000	1.3333	4.0001	56,424.0	18809.0
1	4	5	1.3772	6.3308	8.6255	5.4445
1	4	6	1.3492	6.0582	10.667	6.0250
1	4	7	1.3300	5.8680	12.869	6.6892
1	4	8	1.3162	5.7286	15.228	7.4244
1	4	9	1.3059	5.6227	17.739	8.2227
1	4	10	1.2979	5.5400	20.400	9.0794
1	4	20	1.2667	5.2013	54.705	20.391
1	4	50	1.2538	5.0486	231.29	79.199
1	4	100	1.2512	5.0155	738.28	248.18
1	4	300	1.2502	5.0023	5,020.9	1675.7
1	4	500	1.2501	5.0009	12,520.0	4175.6
1	4	1,000	1.2500	5.0003	43,979.0	14661.0
1	5	6	1.3038	7.6145	9.8349	6.2511
1	5	7	1.2841	7.3327	11.785	6.8008
1	5	8	1.2698	7.1249	13.864	7.4198
1	5	9	1.2591	6.9661	16.069	8.0983
1	5	10	1.2508	6.8414	18.397	8.8300
1	5	20	1.2180	6.3225	48.043	18.528
1	5	50	1.2041	6.0802	198.00	68.430
1	5	100	1.2013	6.0260	623.89	210.37
1	5	300	1.2002	6.0040	4,186.8	1,398.0
1	5	500	1.2001	6.0016	10,396.0	3,467.7
1	5	1,000	1.2000	6.0005	36,349.0	12,118.0
1	6	7	1.2544	8.8954	11.065	7.0718
1	6	8	1.2397	8.6071	12.955	7.6009
1	6	9	1.2287	8.3860	14.952	8.1892
1	6	10	1.2201	8.2115	17.055	8.8289
1	6	20	1.1859	7.4754	43.525	17.395
1	6	50	1.1711	7.1214	175.29	61.195

Table II (*Continued*)

a_1	a_2	a_3	$\alpha_e(11)/V_p$	$\alpha_e(22)/V_p$	$\alpha_e(33)/V_p$	$[\sigma]_\infty$
1	6	100	1.1681	7.0399	545.81	184.67
1	6	300	1.1669	7.0062	3,618.4	1,208.8
1	6	500	1.1667	7.0025	8,950.0	2,986.0
1	6	1,000	1.1667	7.0007	31,163.0	10,390.0
1	7	8	1.2188	10.174	12.308	7.9005
1	7	9	1.2075	9.8815	14.155	8.4148
1	7	10	1.1987	9.6498	16.094	8.9809
1	7	20	1.1632	8.6607	40.253	16.692
1	7	50	1.1477	8.1728	158.74	56.021
1	7	100	1.1444	8.0576	488.85	166.01
1	7	300	1.1431	8.0091	3,204.4	1,071.2
1	7	500	1.1429	8.0037	7,897.7	2,635.6
1	7	1,000	1.1429	8.0011	27,395.0	9,134.8
1	8	9	1.1920	11.452	13.558	8.7343
1	8	10	1.1830	11.155	15.373	9.2375
1	8	20	1.1464	9.8790	37.772	16.265
1	8	50	1.1301	9.2348	146.10	52.157
1	8	100	1.1266	9.0792	445.32	151.84
1	8	300	1.1252	9.0126	2,888.4	966.19
1	8	500	1.1251	9.0052	7,095.0	2,368.3
1	8	1,000	1.1250	9.0015	24,524.0	8,178.2
1	9	10	1.1710	12.728	14.814	9.5714
1	9	20	1.1335	11.130	35.824	16.029
1	9	50	1.1165	10.307	136.12	49.182
1	9	100	1.1128	10.105	410.89	140.70
1	9	300	1.1114	10.017	2,638.5	883.23
1	9	500	1.1112	10.007	6,460.9	2,157.3
1	9	1,000	1.1111	10.002	22,259.0	7,423.5
1	10	20	1.1233	12.415	34.255	15.931
1	10	50	1.1057	11.392	128.01	46.839
1	10	100	1.1018	11.135	382.90	131.71
1	10	300	1.1003	11.022	2,435.6	815.92
1	10	500	1.1001	11.009	5,946.4	1,986.1
1	10	1,000	1.1000	11.002	20,423.0	6,811.8
1	20	50	1.0579	22.911	89.896	37.955
1	20	100	1.0527	21.715	250.13	90.969
1	20	300	1.0504	21.128	1,473.0	498.42
1	20	500	1.0502	21.055	3,510.9	1,177.6
1	20	1,000	1.0501	21.016	11,763.0	3,928.3
1	50	100	1.0243	57.057	161.17	73.084
1	50	300	1.0208	52.284	819.03	290.78
1	50	500	1.0203	51.582	1,860.8	637.82
1	50	1,000	1.0201	51.188	5,938.5	1,996.9
1	100	300	1.0112	107.87	568.97	225.95
1	100	500	1.0105	104.30	1,226.9	444.09
1	100	1000	1.0102	102.14	3,708.3	1,270.5
1	300	500	1.0043	345.37	744.03	363.47
1	300	1,000	1.0037	318.56	1,984.9	768.18
1	500	1,000	1.0024	559.34	1,589.2	716.52
1	1,000	500	1.0024	1589.0	559.36	716.47

TABLE III
Components of the Magnetic Polarizability Tensor α_m for Triaxial Ellipsoids

a_1	a_2	a_3	$\alpha_m(11)/V_p$	$\alpha_m(22)/V_p$	$\alpha_m(33)/V_p$	$[\sigma]_0$
1	2	3	2.3615	1.3645	1.1852	1.6371
1	2	4	2.5181	1.3981	1.1265	1.6809
1	2	5	2.6229	1.4203	1.0932	1.7122
1	2	6	2.6965	1.4357	1.0722	1.7348
1	2	7	2.7501	1.4469	1.0579	1.7516
1	2	8	2.7903	1.4553	1.0476	1.7644
1	2	9	2.8213	1.4618	1.0400	1.7744
1	2	10	2.8457	1.4669	1.0342	1.7823
1	2	20	2.9455	1.4880	1.0116	1.8151
1	2	50	2.9879	1.4972	1.0025	1.8292
1	2	100	2.9963	1.4991	1.0007	1.8321
1	2	300	2.9994	1.4998	1.0001	1.8332
1	2	500	2.9997	1.4999	1.0000	1.8333
1	2	1000	2.9999	1.4999	1.0000	1.8333
1	3	4	3.0083	1.2474	1.1548	1.8035
1	3	5	3.1988	1.2642	1.1155	1.8595
1	3	6	3.3393	1.2764	1.0904	1.9020
1	3	7	3.4455	1.2854	1.0731	1.9347
1	3	8	3.5277	1.2924	1.0606	1.9603
1	3	9	3.5926	1.2979	1.0512	1.9806
1	3	10	3.6447	1.3023	1.0440	1.9971
1	3	20	3.8682	1.3214	1.0154	2.0684
1	3	50	3.9698	1.3304	1.0035	2.1013
1	3	100	3.9907	1.3324	1.0010	2.1081
1	3	300	3.9986	1.3332	1.0001	2.1107
1	3	500	3.9994	1.3332	1.0000	2.1109
1	3	1000	3.9998	1.3333	1.0000	2.1111
1	4	5	3.6510	1.1875	1.1311	1.9899
1	4	6	3.8638	1.1976	1.1034	2.0550
1	4	7	4.0303	1.2054	1.0842	2.1067
1	4	8	4.1626	1.2114	1.0702	2.1481
1	4	9	4.2694	1.2163	1.0597	2.1818
1	4	10	4.3568	1.2202	1.0515	2.2095
1	4	20	4.7497	1.2380	1.0186	2.3354
1	4	50	4.9407	1.2469	1.0043	2.3974
1	4	100	4.9816	1.2490	1.0013	2.4107
1	4	300	4.9973	1.2498	1.0001	2.4158
1	4	500	4.9989	1.2499	1.0000	2.4163
1	4	1000	4.9997	1.2499	1.0000	2.4166
1	5	6	4.2917	1.1511	1.1131	2.1854
1	5	7	4.5202	1.1579	1.0927	2.2570
1	5	8	4.7063	1.1632	1.0777	2.3158
1	5	9	4.8595	1.1676	1.0663	2.3645
1	5	10	4.9869	1.1711	1.0574	2.4052
1	5	20	5.5872	1.1878	1.0212	2.5988
1	5	50	5.8990	1.1968	1.0050	2.7003
1	5	100	5.9683	1.1989	1.0016	2.7230
1	5	300	5.9953	1.1998	1.0002	2.7318
1	5	500	5.9981	1.1999	1.0000	2.7327
1	5	1,000	5.9994	1.1999	1.0000	2.7332
1	6	7	4.9312	1.1266	1.0993	2.3857
1	6	8	5.1714	1.1314	1.0836	2.4622
1	6	9	5.3727	1.1353	1.0716	2.5266
1	6	10	5.5428	1.1386	1.0622	2.5813
1	6	20	6.3796	1.1544	1.0235	2.8525
1	6	50	6.8434	1.1633	1.0057	3.0042

Table III (*Continued*)

a_1	a_2	a_3	$\alpha_m(11)/V_p$	$\alpha_m(22)/V_p$	$\alpha_m(33)/V_p$	$[\sigma]_0$
1	6	100	6.9502	1.1655	1.0018	3.0392
1	6	300	6.9926	1.1664	1.0002	3.0531
1	6	500	6.9970	1.1665	1.0001	3.0546
1	6	1,000	6.9991	1.1666	1.0000	3.0553
1	7	8	5.5700	1.1090	1.0884	2.5891
1	7	9	5.8192	1.1125	1.0760	2.6693
1	7	10	6.0327	1.1156	1.0662	2.7382
1	7	20	7.1272	1.1305	1.0254	3.0944
1	7	50	7.7726	1.1394	1.0063	3.3061
1	7	100	7.9269	1.1416	1.0020	3.3569
1	7	300	7.9890	1.1426	1.0003	3.3774
1	7	500	7.9956	1.1427	1.0001	3.3795
1	7	1,000	7.9987	1.1428	1.0000	3.3805
1	8	9	6.2083	1.0956	1.0796	2.7945
1	8	10	6.4647	1.0984	1.0695	2.8776
1	8	20	7.8308	1.1126	1.0271	3.3236
1	8	50	8.6858	1.1214	1.0068	3.6047
1	8	100	8.8978	1.1237	1.0022	3.6746
1	8	300	8.9846	1.1248	1.0003	3.7032
1	8	500	8.9937	1.1249	1.0001	3.7063
1	8	1,000	8.9982	1.1249	1.0000	3.7077
1	9	10	6.8463	1.0852	1.0723	3.0013
1	9	20	8.4920	1.0987	1.0287	3.5398
1	9	50	9.5822	1.1074	1.0074	3.8990
1	9	100	9.8625	1.1098	1.0024	3.9916
1	9	300	9.9790	1.1109	1.0003	4.0301
1	9	500	9.9915	1.1110	1.0001	4.0342
1	9	1,000	9.9975	1.1110	1.0000	4.0362
1	10	20	9.1126	1.0876	1.0300	3.7434
1	10	50	10.461	1.0962	1.0078	4.1885
1	10	100	10.820	1.0986	1.0026	4.3073
1	10	300	10.972	1.0997	1.0004	4.3576
1	10	500	10.988	1.0999	1.0001	4.3630
1	10	1,000	10.996	1.0999	1.0000	4.3656
1	20	50	18.258	1.0456	1.0112	6.7718
1	20	100	19.980	1.0482	1.0040	7.3444
1	20	300	20.829	1.0496	1.0006	7.6267
1	20	500	20.929	1.0498	1.0002	7.6599
1	20	1,000	20.979	1.0499	1.0000	7.6764
1	50	100	42.139	1.0178	1.0062	14.721
1	50	300	49.147	1.0194	1.0012	17.056
1	50	500	50.191	1.0197	1.0005	17.404
1	50	1,000	50.751	1.0199	1.0001	17.590
1	100	300	90.683	1.0093	1.0017	30.898
1	100	500	96.135	1.0096	1.0008	32.715
1	100	1,000	99.404	1.0098	1.0002	33.805
1	300	500	235.88	1.0029	1.0013	79.295
1	300	1,000	274.51	1.0031	1.0005	92.172
1	500	1,000	413.72	1.0017	1.0006	138.58

increase in simple proportion to volume (molecular weight) for homologous molecular series, since the change in shape will not appreciably affect the intrinsic conductivity. This effect is observed in gas-phase polarizability estimates on normal alkanes, based on dielectric constant and refractive index measurements [43]. Corresponding gas-phase measurements on conjugated polymeric systems, on the other hand, exhibit a rapidly increasing polarizability with molecular weight [43], in accord with the calculations of $\boldsymbol{\alpha}_e$ and the simplistic view of such polymers as "conductors." The variation of the colors of dyes with molecular weight [95] and certain attractive forces between long chain molecules [96] can be similarly understood using this kind of picture of insulating and conducting polymers and geometrical estimates of the polarizability.

There are other shapes for which $\boldsymbol{\alpha}_e$ and $\boldsymbol{\alpha}_m$ can be determined exactly. Most of these additional exact results are summarized by Schiffer and Szegö [46], but are not well known in the physical science literature. (This is probably due to the rather complicated mathematical form of these exact analytical results.) As an example, we indicate exact $\boldsymbol{\alpha}_e$ results, per unit particle volume, for a torus in Fig. 2.3, where the symbol L again denotes the axis of symmetry. The abscissa is the ratio of the overall torus radius b to the radius a of the tube forming the body of the torus itself. For example, the limit $a \to 0$ for a fixed torus radius b gives an infinitely thin wire ring. Table IV tabulates the corresponding numerical values of the polarizability components used in Fig. 2.3, based on previous tabulations of the equivalent of these numbers by Belovitch and Boersma [97]. The present tabulation is given in a dimensionless form that avoids the problem of the choice of units. Further tabulations of analytic results for the electric and magnetic polarizability tensors, corresponding to other shapes [46], will require careful numerical work.

III. INTRINSIC VISCOSITY AND ITS RELATION TO INTRINSIC CONDUCTIVITY

An increase of the viscosity of suspensions and the shear modulus of solids is generally observed upon adding rigid particles to the medium. The introduction of rigid inclusions perturbs the stress field of the sheared pure medium since locally the field lines cannot penetrate the hard inclusions. There is evidently a qualitative analogy with the electrical conduction problem in a suspension of highly conducting particles where the electric field lines are similarly screened from the interiors of the conducting particles. Many authors have commented on the mathematical resemblance between electrical polarization and linearized flow theory calculations [7, 98, 99], which follow as a consequence of this physical

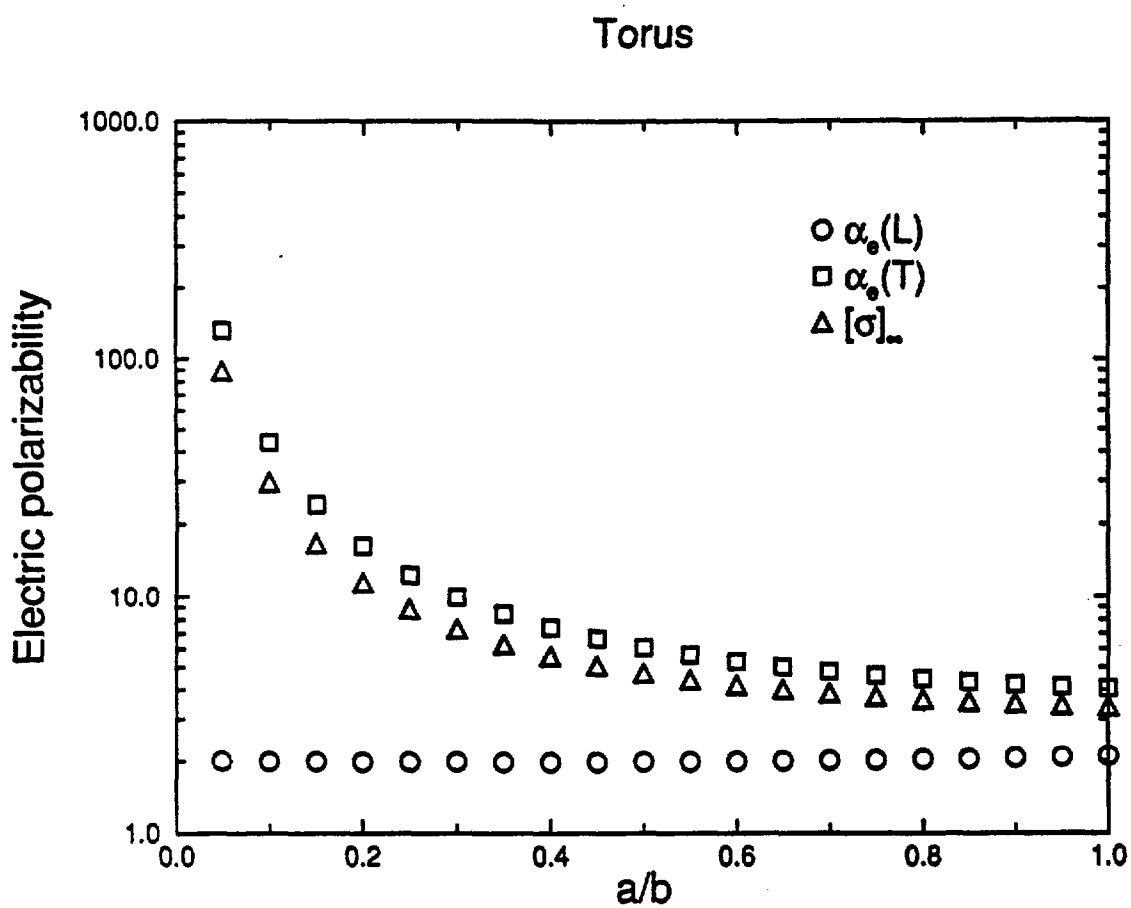

Figure 2.3. The longitudinal (L) and transverse (T) components of the dimensionless (normalized by the particle volume) electric polarizability tensor α_e for tori and the average of these components, the intrinsic conductivity $[\sigma]_\infty$, plotted versus the ratio a/b where b is the overall radius of the torus and a is the radius of the torus tube. The ratio $a/b = 1$ corresponds to a torus without a hole.

analogy. In the following we develop an *approximate* relation between the electrical conductivity and suspension viscosity problems.

Einstein [10a], as part of his investigation of the molecular nature of matter, first calculated the incremental increase of the viscosity η of a dilute hard sphere suspension:

$$\eta/\eta_0 = 1 + (\tfrac{5}{2})\phi + O(\phi^2) \tag{3.1}$$

where η_0 is the pure solution viscosity. (Notably, his original calculation did not give the correct $\frac{5}{2}$ coefficient [10a] in Eq. (3.1) and was later corrected in light of experimental observations by Bancelin [100].) The leading virial coefficient is the intrinsic viscosity $[\eta]$, defined by

$$[\eta] \equiv \lim_{\phi \to 0^+} (\eta - \eta_0)/(\eta_0 \phi) \tag{3.2}$$

TABLE IV
Electric Polarizability Components for Torus

a/b	$\alpha_e(L)/V_p$	$\alpha_e(T)/V_p$	$[\sigma]_\infty$
0.05	1.998	131.851	88.567
0.10	1.995	43.641	29.759
0.15	1.991	24.051	16.698
0.20	1.986	16.282	11.517
0.25	1.983	12.313	8.870
0.30	1.980	9.971	7.307
0.35	1.978	8.455	6.296
0.40	1.977	7.409	5.598
0.45	1.978	6.651	5.093
0.50	1.980	6.083	4.716
0.55	1.985	5.645	4.425
0.60	1.991	5.300	4.197
0.65	1.999	5.024	4.016
0.70	2.008	4.799	3.869
0.75	2.020	4.614	3.750
0.80	2.033	4.461	3.652
0.85	2.047	4.333	3.571
0.90	2.063	4.226	3.505
0.95	2.079	4.135	3.450
0.96	2.083	4.118	3.440
0.97	2.086	4.103	3.431
0.98	2.090	4.087	3.422
0.99	2.094	4.073	3.413
1.00	2.097	4.058	3.405

Experiments on nearly spherical particles in low-concentration suspensions [$\phi < O(1\%)$] commonly yield a value of $[\eta] \approx 2.7$, which is slightly higher [101] than the Einstein estimate $[\eta] = 2.5$. This small deviation is often ascribed to small particle asphericity or particle clustering [101] and, at any rate, the revised Einstein result [Eq. (3.1)] is a good approximation.

Rayleigh [102], Goodier [17], and Hill and Power [103] pointed out a fundamental analogy between the hydrodynamics of suspensions and the elastostatics of incompressible solids with rigid inclusions, which implies that Einstein's virial expansion for the viscosity of hard sphere suspensions also describes the shear modulus G virial expansion [17, 19],

$$G/G_0 = 1 + (\tfrac{5}{2})\phi + O(\phi^2) \tag{3.3}$$

for an elastic continuum of modulus G_0 containing stiff *spherical* inclu-

sions at low concentration. The intrinsic shear modulus $[G]$ is defined by the limit,

$$[G] \equiv \lim_{\phi \to 0^+} (G - G_0)/(G_0 \phi) \tag{3.4}$$

For compressible spherical particles $[G]$ depends on the Poisson ratio ν of the particle [20],

$$[G] = (\tfrac{5}{2})(1 - 2\Delta\nu)/(1 - 10\Delta\nu/3), \qquad \Delta\nu = \nu - \tfrac{1}{2} \tag{3.5}$$

where $\nu \to \frac{1}{2}$ in the incompressible limit. Derivation of Eq. (3.5) assumes that the matrix material always remains in contact with the inclusion ("sticks") under deformation. A tabulation of experiments from a variety of sources indicates that the shear modulus and suspension viscosity have a common concentration dependence [104],

$$G(\phi)/G_0 \approx \eta(\phi)/\eta_0 \tag{3.6}$$

for nearly spherical, rigid inclusions in an incompressible elastic matrix and a Newtonian fluid, respectively. This behavior is consistent with the simple incompressibility assumption ($\nu = \frac{1}{2}$) and the viscoelastic and elastostatic analogy of Rayleigh [102]. It is emphasized that Eq. (3.6) is observed to hold *regardless of the concentration* of the suspended matter! We note that the simple relation between intrinsic viscosity and intrinsic shear modulus is limited to *spherical* particles and an incompressible suspending medium (see Appendix C).

Experience also indicates that the addition of "softer" materials to liquids and solids does not generally increase the viscosity and shear modulus. This physical situation is analogous to the addition of insulating material to a conducting medium [42a], since the inclusions are "permeable" to the shear-induced stress field lines in the suspending fluid or solid medium. In the extreme case, where the particle inclusions are highly deformable and the matrix is incompressible, $[G]$ becomes [18]

$$[G]_{d=3} = -\tfrac{5}{3}, \qquad [G]_{d=2} = -2 \tag{3.7}$$

so that the solid becomes *softer* with an increasing volume fraction of soft inclusions. The magnitude of $[G]$ for holes is comparable to $[\sigma]_0$ for an insulator in a conducting matrix [see Eq. (2.1)].

The introduction of liquid drops into another viscous fluid or a solid introduces some important additional features. In this case, momentum can propagate into the interior of the droplet and induce internal circulation within the droplet, so that the dissipation is altered from the

hard sphere case. In many physical circumstances surface tension or internal pressure tends to make the drop resist deformation, however. Taylor [15] showed that the intrinsic viscosity of idealized *indeformable* liquid drops of viscosity η_{drop} equals

$$[\eta] = 1 + \tfrac{3}{2}[z_\eta/(1+z_\eta)], \qquad z_\eta = \eta_{\text{drop}}/\eta_0 \tag{3.8}$$

Note that $[\eta]$ reduces to 1 in the "bubble" limit $z_\eta \to 0^+$, rather than becoming negative. Experiments on liquid drops suspended in another liquid are often consistent with Eq. (3.8), although there can be complications with surface tension effects (impurities and small droplet size [105]), which can invalidate Eq. (3.8). In the complementary idealized case, where the spherical membrane surrounding the droplet is highly deformable, it is found that [106]

$$[\eta] = -\tfrac{5}{3}[1 - \tfrac{5}{3}z_\eta/(1+\tfrac{2}{3}z_\eta)] \tag{3.9}$$

which reduces to the hole limit $-\frac{5}{3}$ for the elastic problem [Eq. (3.7)] for $z_\eta \to 0$ and the *hard sphere* result ($z_\eta \to \infty$) of Einstein. Equation (3.9), which is comparable to Maxwell's formula [Eq. (2.1a)] for electrical conductivity, has been found to be a reasonable idealization for suspensions of red blood cells and other deformable particles [106]. The rest of this chapter considers only *rigid* particles. The brief discussion above was meant only to illustrate some of the complications that can arise when considering real particle mixtures.

Despite the fundamental importance of $[\eta]$ in determination of molecular shape [107], there are few analytical calculations of $[\eta]$ corresponding to nonspherical objects. Onsager [11] long ago calculated asymptotic results for long hard prolate ellipsoids, and these results were later generalized by Saito [12a] to analytical estimates for arbitrary aspect ratios. Kirkwood and Riseman [108] and Debye and Bueche [109] estimated $[\eta]$ for random coil polymer chains, but these calculations involved uncontrolled approximations. Rallison [13] and Haber and Brenner [14] recently obtained exact results for *triaxial* ellipsoids. The formalism required to treat the triaxial ellipsoid case is quite sophisticated and treatment of these more general shapes is necessarily complicated. The reason for the limited progress in calculating $[\eta]$, relative to $[\sigma]$, is simple: Solution of the steady-state Navier–Stokes equation on the exterior of the hard particles is a significantly more difficult technical problem than the corresponding solution of the Laplace equation.

Recently, Hubbard and Douglas [27] observed an interesting relation between hydrodynamic and electrostatic problems that suggests a route

for developing a direct approximate relation between $[\eta]$ and $[\sigma]$. They observed that the *angular average* of the Green's function for the steady-state free space Navier–Stokes equation equals the Green's function of the free space Laplacian [27]. From this observation and the physical *angular averaging* associated with the Brownian particle diffusion process, they deduced that the scalar translational friction coefficient of arbitrarily shaped rigid paricles approximately equals

$$f_T \approx 6\pi\eta C \tag{3.10}$$

where C is the electrostatic capacitance. (The parameter C is the Newtonian capacity as opposed to the logarithmic capacity discussed in Section V. The units of C are chosen so that a sphere of radius R has a capacitance $C = R$.) The capacitance C governs the far field decay of the solution of Laplace's equation where the solution equals 1 on the boundary and approaches zero at great distances from the boundary [26, 80]. Equation (3.10), which is consistent (within ~1% accuracy) with exactly known values of f_T, serves as an explicit connection between hydrodynamic and electrostatic problems. Direct comparisons of the average stress and electrostatic (or thermal) dipole coefficients [110–112] in the calculation of $[\eta]$ and $[\sigma]_\infty$, respectively, suggests that $[\eta]$ is simply proportional to $[\sigma]_\infty$ within angular averaging. In other words, it seems reasonable to preangularly average the steady-state Navier–Stokes Green's function so that the hydrodynamic problem reduces to the solution of the Laplace equation on the exterior of the particle as in the former calculations relating translational friction and capacity [27]. This procedure seems reasonable for a dilute particle suspension of randomly oriented particles, since $[\eta]$ is then an invariant under suspension rotations. In this chapter we are interested in checking the numerical accuracy of this relation. The existence of small numerical discrepancies in exact analytical results, described below, show that this relation is not exact, but rather a very good approximation for objects having diverse shapes.

The constant of proportionality between $[\eta]$ and $[\sigma]_\infty$ can be fixed by exact calculations for sphere suspensions [5, 113] in d spatial dimensions

$$[\eta] \approx [(d+2)/(2d)][\sigma]_\infty \tag{3.11}$$

We choose the sphere case to determine the proportionality constant since the preaveraging argument for the Oseen tensor leads to exact results for spheres. Of course, this is a rather trivial case and other shapes must be considered to check the conjectured relation [Eq. (3.11)] [114].

Further motivation of the approximation [Eq. (3.11)], derives from

calculations by Kanwal [115], which show an *exact* relation between the rotational friction coefficient f_R and α_e for a certain class of bodies

$$f_R(T) = 2\alpha_e(T)\eta_0 \tag{3.12}$$

corresponding to the rotation of a body of revolution, having an otherwise arbitrary profile, about its axis of symmetry. The parameter $\alpha_e(T)$ is the polarizability component normal to the axis of symmetry. Exact $f_R(T)$ results for a variety of complex-shaped particles can be directly obtained from Eq. (3.12) and from tabulations of $\alpha_e(T)$ [46].

Riseman and Kirkwood [116] noted that a proportionality relation should exist between the rotational friction coefficient and $[\eta]$, and this observation is consistent with the approximation in Eqs. (3.11) and (3.12). The rotational friction coefficient becomes difficult to measure and to calculate for nonsymmetric objects and for flexible objects so we do not pursue this connection further.

Brenner [117] developed the necessary mathematical machinery for calculating $[\eta]$ for rigid axisymmetric particles. It is useful to utilize this formalism to obtain some exact results that can be tested against Eq. (3.11). The particle shape made from two touching spheres of radius a is an interesting test case. Exact calculation, using the formalism of Brenner [117] and associated results for the stress dipole due previously to Wakiya [118], gives an *exact* value for the intrinsic viscosity of two touching and rigidly joined spheres

$$[\eta] = 3.4496\cdots \tag{3.13}$$

(We note that the value of $[\eta]$ given on p. 263 of [117] is incorrect.) An exact calculation of α_e (and thus implicitly $[\sigma]_\infty$) for touching spheres is summarized by Schiffer and Szegö [46]. The electrical polarizability components along the symmetry axis $\alpha_e(L)$ and normal to the symmetry axis $\alpha_e(T)$ equal

$$\alpha_e(L) = 16\pi a^3\zeta(3), \qquad \alpha_e(T) = 6\pi a^3\zeta(3) \tag{3.14a}$$

where ζ is the Riemann zeta function, that is $\zeta(3) = 1.20206\cdots$. The intrinsic conductivity $[\sigma]_\infty$ for touching spheres is then

$$[\sigma]_\infty = 7\zeta(3)/2 = 4.2072\cdots, \qquad V_p = 8\pi a^3/3 \tag{3.14b}$$

Equations (3.13) and (3.14) imply that the ratio $[\eta]/[\sigma]$ for touching spheres equals

$$[\eta]/[\sigma]_\infty = 0.820\cdots \tag{3.15}$$

which agrees well with the estimate from Eq. (3.11)

$$[\eta]/[\sigma]_\infty = \tfrac{5}{6} = 0.833\cdots \tag{3.16}$$

We also compare the exact result to recent bead model calculations of $[\eta]$ for touching spheres by de la Torre and Bloomfield [119]. They find $[\eta] = 3.493$ for touching spheres, which is accurate to within 1% in comparison with the exact result [Eq. (3.13)].

Exact polarizability results are also known for the disk and needle limits of an ellipsoid of revolution. For a disk of radius a the polarizability components [46] and $[\sigma]_\infty$ in number density units equal

$$\alpha_e(L) = 0, \qquad \alpha_e(T) = 16a^3/3, \qquad [\sigma]_\infty = 32a^3/9 \tag{3.17}$$

and from the formalism of Brenner [117] we can also obtain an exact calculation of the intrinsic viscosity of a disk as

$$[\eta] = 128a^3/45 \tag{3.18}$$

which is also given in number density units. This result is probably known but we could not find a reference to it. For a disk we then obtain the exact ratio

$$[\eta]/[\sigma]_\infty = 0.8 \tag{3.19}$$

which is rather close to the approximation [Eq. (3.11)].

In the opposite *needle limit* ($x \to \infty$), corresponding to an extended prolate ellipsoid, the asymptotic scaling of $[\sigma]_\infty$ with x can be deduced analytically

$$[\sigma]_\infty \sim \tfrac{1}{3}x^2/\log(x) \tag{3.20}$$

where x is the ratio of the semimajor axis length to the semiminor axis length. Onsager [11] calculated the corresponding asymptotic prolate ellipsoid result for $[\eta]$ as

$$[\eta] \sim \tfrac{4}{15}x^2/\log(x) \tag{3.21}$$

which is consistent with more general calculations given later by Saito [12]. The exact limiting ratio for $[\eta]/[\sigma]_\infty$ for a *needle* ($x \to \infty$) then equals

$$[\eta]/[\sigma]_\infty = 0.8 \tag{3.22}$$

which is *identical* to the ratio obtained for a disk. The ratio $[\eta]/[\sigma]_\infty$ is thus found to be *nearly invariant* for a significant range of particle shapes, as expected from Eq. (3.11). In Fig. 2.4a we plot log $[\eta]$ versus log $[\sigma]_\infty$ for a wide range of aspect ratios for prolate ellipsoids of revolution, while Fig. 2.4b shows a similar graph for oblate ellipsoids of revolution, where the abscissa is now the inverse of the aspect ratio. The straight line is a fit that gives an average value of 0.8 for the intrinsic viscosity/conductivity ratio. Table V gives the numerical data shown in Fig. 2.4, where the $[\eta]$ results are taken from the original tabulation of Scheraga [120a].

The information required to obtain $[\eta]$ for triaxial ellipsoids is also known, although this information is rather inaccessible because of the complicated mathematical formalism that these calculations involve. The necessary formulas for the components of the electric polarizability [52a] are summarized in Appendix B and a summary of the necessary results of Haber and Brenner [14] for $[\eta]$ are provided in Appendix C. Tabulations

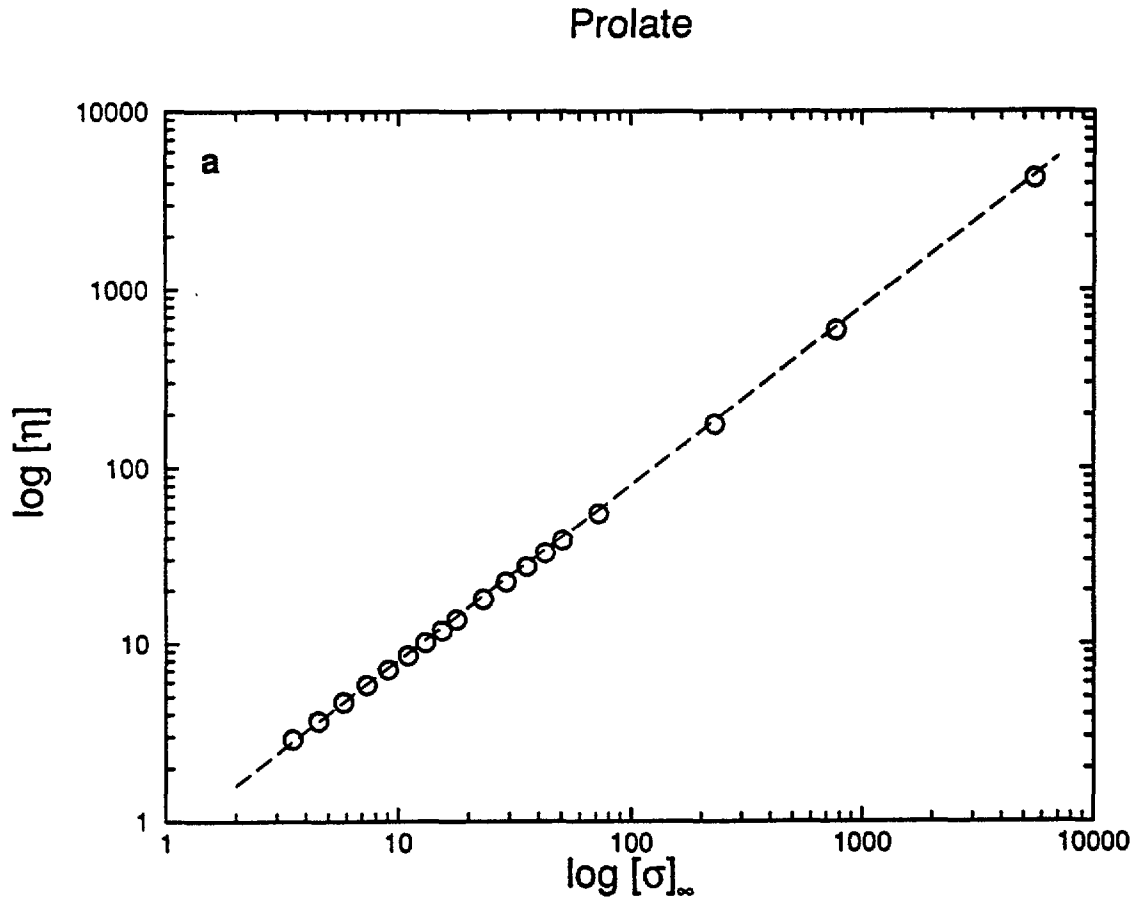

Figure 2.4. The intrinsic viscosity $[\eta]$ versus the intrinsic conductivity $[\sigma]_\infty$ for ellipsoids of revolution. The scales are logarithmic (base 10): (a) prolate and (b) oblate.

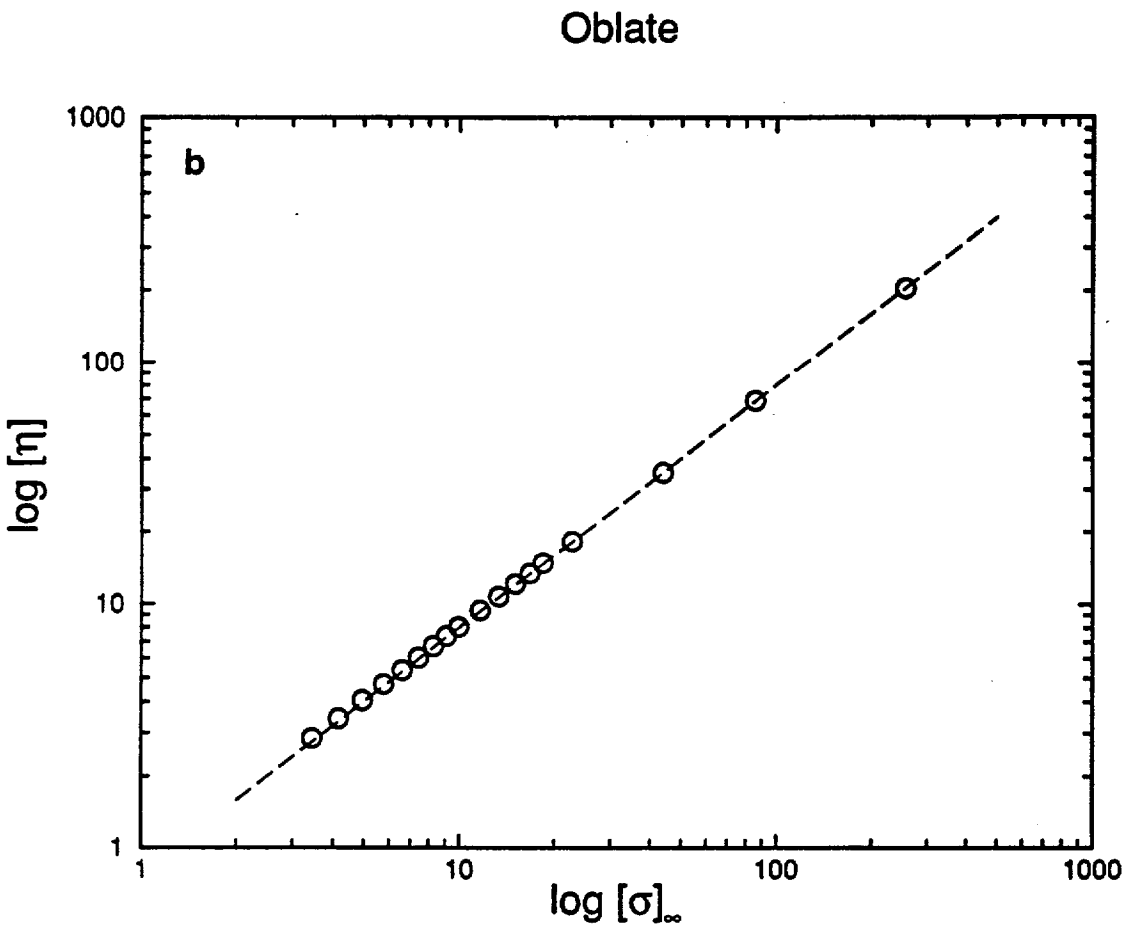

Figure 2.4. (*Continued*)

of these virial coefficients, which should be useful in applications, are given in Table VI.

We observe from Tables V and VI that all the ellipsoid data is nearly consistent with the ratio given in Eq. (3.16)

$$[\eta]/[\sigma]_\infty = 0.79 \pm 0.04 \tag{3.23}$$

so that $[\eta]/[\sigma]_\infty$ is an *invariant* to within a 5% accuracy. The angular averaging approximation is not as accurate for $[\eta]$ as in previous applications to f_T [27, 80], but Eq. (3.16) is sufficiently accurate for many practical applications since measurement and numerical calculation errors are often comparable to the 5% inaccuracy indicated by Eq. (3.23).

Equation (3.23) also holds for the spherical *dumbbell* at arbitrary separations. The dumbbell is defined by two identical spheres connected by a straight wire of zero thickness and fixed length. In the calculation of the polarizability the spheres are uncharged and the wire has zero

TABLE V
Intrinsic Viscosity and Intrinsic Conductivity for Ellipsoids of Revolution

Aspect Ratio $(x, 1/x)$	Prolate			Oblate		
	$[\sigma]_\infty$	$[\eta]$	$[\eta]/[\sigma]_\infty$	$[\sigma]_\infty$	$[\eta]$	$[\eta]/[\sigma]_\infty$
2	3.5339	2.908	0.82	3.4524	2.854	0.83
3	4.5622	3.685	0.81	4.1815	3.431	0.82
4	5.8625	4.663	0.80	4.9728	4.059	0.82
5	7.3836	5.806	0.79	5.7878	4.708	0.81
6	9.1043	7.099	0.78	6.6145	5.367	0.81
7	11.013	8.533	0.77	7.4476	6.032	0.81
8	13.101	10.10	0.77	8.2847	6.700	0.81
9	15.362	11.80	0.77	9.1245	7.371	0.81
10	17.793	13.63	0.77	9.9661	8.043	0.81
12	23.146	17.67	0.76	11.653	9.391	0.81
14	29.134	22.19	0.76	13.343	10.74	0.80
16	35.738	27.18	0.76	15.035	12.10	0.80
18	42.942	32.63	0.76	16.728	13.45	0.80
20	50.732	38.53	0.76	18.422	14.80	0.80
25	72.701	55.19	0.76	22.660	18.19	0.80
50	232.34	176.8	0.76	43.868	35.16	0.80
100	776.71	593.7	0.76	86.303	69.10	0.80
300	5,560.0	4,279.0	0.77	256.06	204.9	0.80

electrical resistance, while for the intrinsic viscosity calculation the wire has a vanishing hydrodynmic resistance. Brenner [117] summarized the information required to calculate $[\eta]$ for a dumbbell and an exact calculation of $[\sigma]_\infty$ for the dumbbell is given in Appendix D.

We define the quantity r_p to be the ratio of the distance between the centers of the spheres to their diameters, which completely characterizes the shape of the spherical particle dumbbell. It is then found that the value of $[\eta]$ is approximately quadratic in r_p. A useful approximate formula for $[\eta]$, covering the range $1 < r_p < 10$, is given by

$$[\eta] = 2.5 + (1.037 - 0.3196\lambda) r_p^2$$
$$\lambda = (r_p/3)/(1 + r_p/3) \tag{3.24}$$

which holds to about a 3% accuracy. Exact results for $[\eta]$ are tabulated in Table VII and the asymptotic variation of $[\eta]$ for a dumbbell at large separation equals

$$[\eta] \sim \tfrac{3}{4} r_p^2, \qquad r_p \to \infty \tag{3.25}$$

TABLE VI
Intrinsic Viscosity and Intrinsic Conductivity for Triaxial Ellipsoids

a_1	a_2	a_3	$[\sigma]_\infty$	$[\eta]$	$[\eta]/[\sigma]_\infty$
1	2	3	3.9585	3.2454	0.82
1	2	4	4.6903	3.8027	0.81
1	2	5	5.5723	4.4704	0.80
1	2	6	6.5774	5.2291	0.80
1	2	7	7.6924	6.0695	0.79
1	2	8	8.9098	6.9864	0.78
1	2	9	10.225	7.9765	0.78
1	2	10	11.633	9.0372	0.78
1	2	20	30.436	23.227	0.76
1	2	50	131.53	100.02	0.76
1	2	100	429.47	327.72	0.76
1	2	300	3,006.5	2,309.9	0.77
1	2	500	7,574.0	5,835.8	0.77
1	2	1,000	26,904.0	20,799.0	0.77
1	3	4	4.6662	3.8090	0.82
1	3	5	5.2975	4.2941	0.81
1	3	6	6.0356	4.8572	0.80
1	3	7	6.8626	5.4855	0.80
1	3	8	7.7688	6.1722	0.79
1	3	9	8.7483	6.9133	0.79
1	3	10	9.7970	7.7061	0.79
1	3	20	23.678	18.194	0.77
1	3	50	96.894	73.776	0.76
1	3	100	309.75	236.28	0.76
1	3	300	2,127.6	1,633.2	0.77
1	3	500	5,328.6	4,102.3	0.77
1	3	1,000	18,810.0	14,531.0	0.77
1	4	5	5.4445	4.4297	0.81
1	4	6	6.0250	4.8788	0.81
1	4	7	6.6892	5.3889	0.81
1	4	8	7.4244	5.9506	0.80
1	4	9	8.2227	6.5587	0.80
1	4	10	9.0794	7.2099	0.79
1	4	20	20.391	15.777	0.77
1	4	50	79.199	60.416	0.76
1	4	100	248.18	189.35	0.76
1	4	300	1,675.7	1,285.7	0.77
1	4	500	4,175.7	3,212.9	0.77
1	4	1,000	14,662.0	11,321.0	0.77
1	5	6	6.2511	5.0734	0.81
1	5	7	6.8008	5.5010	0.81
1	5	8	7.4198	5.9787	0.81
1	5	9	8.0983	6.4997	0.80
1	5	10	8.8300	7.0595	0.80
1	5	20	18.528	14.427	0.78
1	5	50	68.430	52.314	0.76
1	5	100	210.37	160.57	0.76
1	5	300	1,398.0	1,072.2	0.77
1	5	500	3,467.8	2,666.9	0.77
1	5	1,000	12,119.0	9,352.9	0.77
1	6	7	7.0718	5.7287	0.81
1	6	8	7.6009	6.1419	0.81
1	6	9	8.1892	6.5978	0.81
1	6	10	8.8289	7.0910	0.80
1	6	20	17.396	13.622	0.78
1	6	50	61.196	46.893	0.77

Table VI (*Continued*)

a_1	a_2	a_3	$[\sigma]_\infty$	$[\eta]$	$[\eta]/[\sigma]_\infty$
1	6	100	184.67	141.03	0.76
1	6	300	1,208.9	926.83	0.77
1	6	500	2,986.1	2,295.6	0.77
1	6	1,000	10,391.0	8,015.9	0.77
1	7	8	7.9005	6.3907	0.81
1	7	9	8.4148	6.7935	0.81
1	7	10	8.9809	7.2337	0.81
1	7	20	16.693	13.136	0.79
1	7	50	56.021	43.030	0.77
1	7	100	166.02	126.88	0.76
1	7	300	1,071.2	821.07	0.77
1	7	500	2,635.6	2,025.5	0.77
1	7	1,000	9,134.8	7,044.6	0.77
1	8	9	8.7343	7.0568	0.81
1	8	10	9.2375	7.4520	0.81
1	8	20	16.266	12.855	0.79
1	8	50	52.157	40.159	0.77
1	8	100	151.85	116.13	0.76
1	8	300	966.19	740.43	0.77
1	8	500	2,368.4	1,819.5	0.77
1	8	1,000	8,178.3	6,304.8	0.77
1	9	10	9.5714	7.7258	0.81
1	9	20	16.030	12.714	0.79
1	9	50	49.182	37.959	0.77
1	9	100	140.70	107.70	0.77
1	9	300	883.23	676.75	0.77
1	9	500	2,157.4	1,657.0	0.77
1	9	1,000	7,423.6	5,721.3	0.77
1	10	20	15.931	12.675	0.80
1	10	50	46.839	36.235	0.77
1	10	100	131.71	100.92	0.77
1	10	300	815.93	625.11	0.77
1	10	500	1,986.2	1,525.1	0.77
1	10	1,000	6,811.8	5,248.3	0.77
1	20	50	37.956	29.929	0.79
1	20	100	90.969	70.422	0.77
1	20	300	498.42	381.99	0.77
1	20	500	1,177.7	903.15	0.77
1	20	1,000	3,928.4	3,020.6	0.77
1	50	100	73.084	57.942	0.79
1	50	300	290.78	224.55	0.77
1	50	500	637.83	490.03	0.77
1	50	1,000	1,996.9	1,532.4	0.77
1	100	300	225.95	177.13	0.78
1	100	500	444.09	344.09	0.77
1	100	1,000	1,270.5	976.50	0.77
1	300	500	363.47	289.19	0.80
1	300	1,000	768.19	600.59	0.78
1	500	1,000	716.53	567.67	0.79

TABLE VII
Selected Values of the Intrinsic Viscosity and Intrinsic Conductivity for the Spherical Dumbbell

r_p	$[\sigma]_\infty$	$[\eta]$	$[\eta]/[\sigma]_\infty$
1.0000	4.2072	3.4496	0.82
1.0201	4.2707	3.4980	0.82
1.1276	4.6180	3.6754	0.80
1.5431	6.0912	4.8914	0.80
3.7622	19.176	14.756	0.77
6.1323	43.856	33.308	0.76
10.0677	109.603	82.690	0.75
$r_p \to \infty$	$3r_p^2/4$	r_p^2	0.75

Simha [120b] previously indicated a quadratic dependence of $[\eta]$ on r_p in the $r_p \to \infty$ limit, but his widely cited value for the prefactor, $\frac{3}{2}$, is not correct. The origin of this discrepancy is not clear, but we note that Simha [120b] ignored hydrodynamic interactions.

Schiffer and Szegö [46] previously summarized exact results for the electric polarizability of two *separated* spheres without the connecting wire. The generation of a large dipole in separated spheres, however, requires the electrical connection and the calculation of $[\sigma]_\infty$ in the case where there is a connecting wire is given in Appendix D. A tabulation of these new results for $[\sigma]_\infty$, along with the dimensionless polarizability components (normalized by the particle volume), is given in Table VII. These results are shown graphically in Fig. 2.5. It is hard to imagine a geometry more representative of a dipole. For large separations $[\sigma]_\infty$ is simply proportional to r_p^2

$$[\sigma]_\infty \sim r_p^2, \qquad r_p \to \infty \tag{3.26}$$

so that we have the asymptotic result

$$[\eta]/[\sigma]_\infty \sim 0.75, \qquad r_p \to \infty \tag{3.27}$$

It is interesting that the dumbbell accords with Eq. (3.23) even in the extreme limit of infinite separation.

We also mention some results for the intrinsic conductivity of insulating dumbbells. From the results of Schiffer and Szegö [46] for the effective mass M of touching spheres and Eq. (2.6) we have

$$\alpha_m(L) = -9\zeta(3)/8 \qquad \text{(touching spheres)} \tag{3.28}$$

and by finite element methods we calculate the other component

TABLE VIII
Electric Polarizability Components for Dumbbell

r_p	$\alpha_e(L)/V_p$	$\alpha_e(T)/V_p$	$[\sigma]_\infty$
1.005	2.70774	7.25347	4.22298
1.050	2.73443	7.62957	4.36615
1.100	2.76139	8.06009	4.52763
1.150	2.78562	8.50399	4.69174
1.200	2.80726	8.96133	4.85862
1.250	2.82651	9.43222	5.02841
1.300	2.84358	9.91671	5.20129
1.350	2.85869	10,4149	5.37743
1.400	2.87207	10.9268	5.55700
1.450	2.88393	11.4526	5.74015
1.500	2.89444	11.9923	5.92705
1.750	2.93207	14.9010	6.92172
2.000	2.95400	18.1651	8.02437
2.250	2.96749	21.7895	9.24149
2.500	2.97622	25.7778	10.5767
2.750	2.98209	30.1325	12.0322
3.000	2.98618	34.8556	13.6093
3.250	2.98912	39.9485	15.3089
3.500	2.99128	45.4122	17.1316
4.000	2.99415	57.4550	21.1478
4.500	2.99589	70.9883	25.6600
5.000	2.99700	86.0150	30.6697
5.500	2.99775	102.537	36.1774
6.000	2.99826	120.555	42.1838
6.500	2.99864	140.070	48.6892
7.000	2.99891	161.084	55.6938
7.500	2.99911	183.595	63.1977
8.000	2.99927	207.605	71.2011
8.500	2.99939	233.114	79.7041
9.000	2.99949	260.121	88.7067
9.500	2.99956	288.628	98.2091
10.000	2.99963	318.634	108.211
20.000	2.99995	1,233.70	413.231
30.000	2.99999	2,748.71	918.237
40.000	2.99999	4,863.72	1,623.24
50.000	3.00000	7,578.73	2,528.24
100.000	3.00000	30,153.7	10,053.2
150.000	3.00000	67,728.7	22,578.2
200.000	3.00000	120,304.0	40,103.2
250.000	3.00000	187,879.0	62,628.2
300.000	3.00000	270,454.0	90,153.2
350.000	3.00000	368,029.0	122,678.0
400.000	3.00000	480,604.0	160,203.0
450.000	3.00000	608,179.0	202,728.0
500.000	3.00000	750,754.0	250,253.0

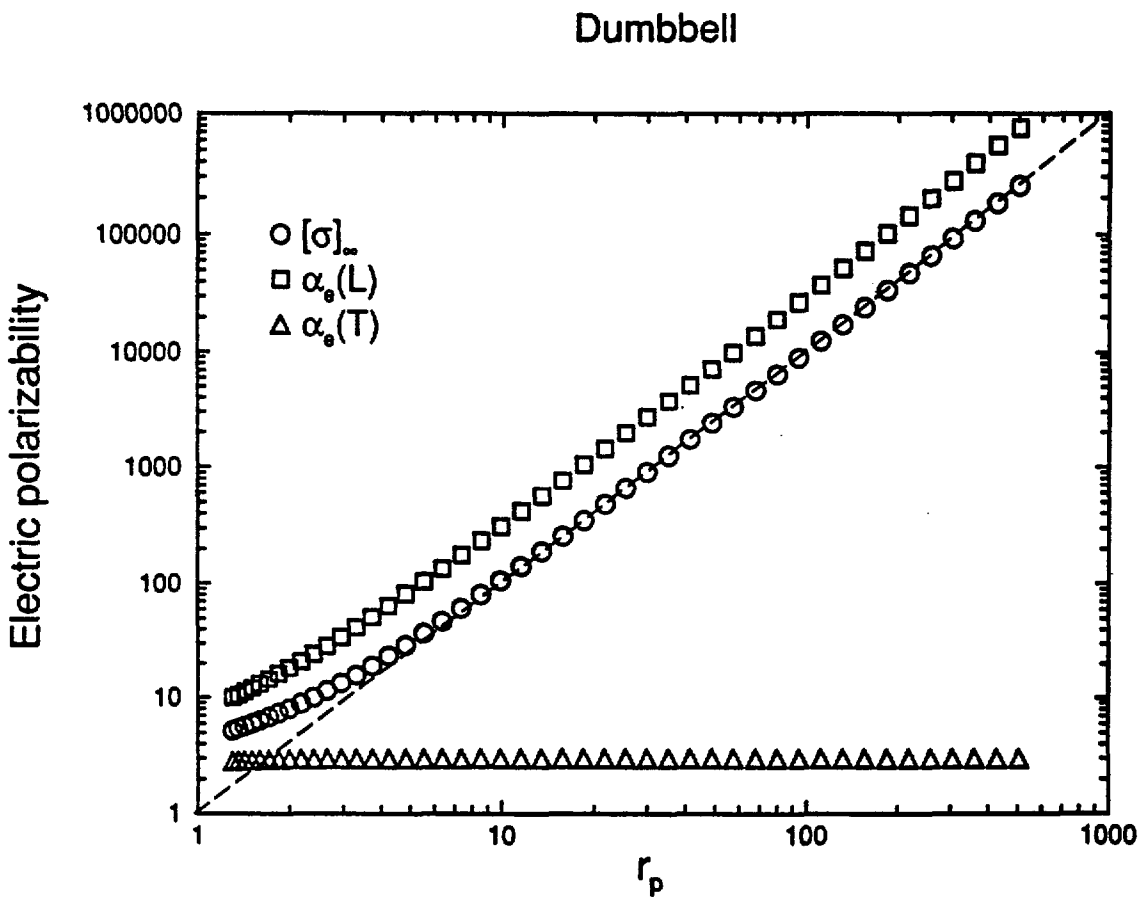

Figure 2.5. Longitudinal (L) and transverse (T) components of the dimensionless (normalized by the particle volume) electric polarizability tensor α_e for the spherical particle dumbbell, along with the average of these components, the intrinsic conductivity $[\sigma]_\infty$.

$$\alpha_m(T) \approx -41\zeta(3)/30 \qquad \text{(touching spheres)} \tag{3.29}$$

which has long defied exact analytical calculation [46]. [The closed form estimate in Eq. (3.29) is based on the assumption that $\alpha_m(T)$ is proportional to $\zeta(3)$, as in Eq. (3.28), in combination with accurate numerical estimates of $\alpha_m(T)$.] We note that the known value of $\alpha_m(L)$ is given by our finite element method to an accuracy of better than 1%, so we expect that the corresponding value for the unknown $\alpha_m(T)$ should be correct within the same tolerance. (From previous experience, the finite element method used here is always more accurate for conducting matrix–insulating particle problems than for conducting matrix–superconducting particle problems.) We then obtain the intrinsic conductivity of the insulating doublet of spheres

$$[\sigma]_0 \approx -(463/360)\zeta(3) = -1.55\cdots \tag{3.30}$$

This value is only slightly different than the sphere result $[\sigma]_0 = -\frac{3}{2}$ of Maxwell [4a] [see Eq. (2.1)]. At large distances between the spheres, the dumbbell should approach the sphere value, so the spatial variation of $[\sigma]_0$ has limited interest in comparison with the conducting dumbbell case. We note that in the insulating case and long slender bodies, $\alpha_m(L)/V_p$ tends to approach -1. This result can be derived from slender body theory using results of Miles [120c] and the known relation between $\alpha_m(L)$ and $\alpha_m(T)$. The corresponding value of $\alpha_m(T)/V_p$ approaches -2, so that $[\sigma]_0$ obeys the general relation

$$[\sigma]_0 = -\tfrac{5}{3} \qquad \text{(slender body)} \tag{3.31}$$

Even in this extreme limit the deviation of $[\sigma]_0$ from the sphere value is unimpressive. The variation of $[\sigma]_0$ with shape is more interesting for flat bodies (see Fig. 2.2). We return to a discussion of flat bodies in Section VI.

As a final point, we mention that exact calculation of $[\eta]$ for other shapes is possible, in principle. Exact results for $\boldsymbol{\alpha}_e$ and $\mathbf{M}$ are known for the lens, bowl, spindle and other shapes [46]. Calculation of $[\eta]$ involves similar (albeit more complicated) mathematics.

IV. NUMERICAL INVESTIGATION OF $[\eta]/[\sigma]_\infty$ RATIO ($d = 3$)

Further examples of the approximate invariance of $[\eta]/[\sigma]_\infty$ for a variety of shapes are given in this section based on numerical finite element computations in combination with partial analytic results for $[\eta]$ and $[\sigma]_\infty$. All of the results obtained are consistent with Eq. (3.23).

The analogy of the elastostatic and hydrodynamic problems of fluid suspensions and solid composites [17, 102, 103], mentioned in Section III, indicates that a modification of existing finite element programs for calculating the effective elastic properties of composite bodies can be made to also obtain $[\eta]$. This modification and the variational principle for obtaining the Stokes' equation on which it is based, are described in Appendix E for particles with orthorhombic symmetry or higher (triaxial ellipsoids have orthorhombic symmetry). We note that Brenner's work [117] was essential in checking the consistency of this generalization, especially in the case of anisotropic elastic stiffness and viscosity tensors. We also utilize a similar finite element program for the calculation of $[\sigma]_\infty$. This finite element method is also described in Appendix E. All particles were represented by a cubical digital image, so that the elements were cubes arrayed on a simple cubic lattice. A standard lattice of size 104^3 was used, which was the largest that would fit in the memory of the

computer available to us and which would allow reasonable running times. Even so, the total CPU time used to compute the results in this chapter was about 2000 h on a CONVEX 3820 supercomputer.

In these numerical calculations, arbitrary shapes had to be represented by collections of pixels. Because of the overall computational cell size limit, a compromise had to be taken between using enough pixels to give a good representation of the particle, and keeping the particle small compared to the overall unit cell, so as to keep the volume fraction small enough to be in the linear regime in concentration. The size and complexity of the objects that could be treated in this fashion is necessarily limited, but a good approximation to a wide range of physically interesting objects could still be obtained.

Periodic boundaries were used in all simulations to reduce the importance of finite size edge effects. Since a cubic cell was always used, in reality all computations were really for simple cubic periodic arrays of the object considered. Exact calculations exist for the intrinsic conductivity and viscosity of rigid spheres arranged on a simple cubic lattice. This example can then be used to illustrate the effect of finite resolution, as described above, and finite system size on the accuracy of the computations.

Zuzovsky and Brenner carried out computations for the effective conductivity of cubic arrays of spheres embedded in a matrix [121a], which are very useful for comparison with our numerical data. For the particular case where the spheres were *superconducting* and the matrix was an ordinary conductor of unit conductivity, they developed an accurate formula for the effective conductivity σ of the composite medium. Subtracting one from the effective conductivity, and dividing by the sphere volume fraction ϕ, gives their prediction for the effective *intrinsic conductivity* at any sphere volume fraction

$$[\sigma]_\infty = 3[1 - \phi - 1.306\phi^{10/3}/(1 - 0.407\phi^{7/3}) - 0.022\phi^{14/3} + O(\phi^6)]^{-1} \tag{4.1}$$

where $\phi = \pi(d/L_c)^3/6$, d = sphere diameter, and L_c = size of cubic unit cell. Actually, this quantity is only equal to the true intrinsic conductivity in the limit where ϕ is small enough so that the expansion in Eq. (2.2b) is applicable. Equation (4.1), however, provides a useful way to represent our numerical conductivity data.

Nunan and Keller [121b] computed the components of the viscosity tensor of the simple cubic array of rigid spheres in a fluid. There are two independent components for this symmetry (there would be three

independent elastic components, but incompressibility reduces these to two), defined by Nunan and Keller as two functions of ϕ, p and q. With the use of their exact numerical results, they were able to show that an analytic expansion given by Zuzovsky et al. [121c] was accurate to within 0.2% up to $\phi = 0.13$ ($d/L_c = 0.63$) for simple cubic sphere packings. This analytic expression equals

$$p = 2.5\phi[1 - (1 - 60b)\phi + 12a\phi^{5/3} + O(\phi^{7/3})]^{-1} \tag{4.2a}$$

$$q = 2.5\phi[1 - (1 + 40b)\phi - 8a\phi^{5/3} + O(\phi^{7/3})]^{-1} \tag{4.2b}$$

where $a = 0.2857$ and $b = -0.04655$. In terms of p and q, the rotationally averaged intrinsic viscosity $[\eta] = (\eta/\eta_0 - 1)/\phi$ at any volume fraction ϕ is given by

$$[\eta] = (2p + 3q)/5 \tag{4.3}$$

Figure 2.6 shows the finite element results for periodic arrays of spheres, along with the exact results, Eqs. (4.1) and (4.3). First, consider the results for the intrinsic viscosity (circles). At small values of d/L_c, the numerical results are well above the exact result. This result is due to not having enough pixels to represent the spherical shape. For example, a sphere with a diameter of five pixels (a pixel is considered to be part of the sphere if its center lies within a radius of the center) does not look much like a smooth continuum sphere. In fact, all the finite element results shown in Fig. 2.6 have been rotationally averaged, as they have cubic symmetry. As d/L_c increases, allowing each sphere to be represented by more pixels, resolution improves, and the numerical points approach the exact curve. There is a region, around $d/L_c = 0.4$, where the numerical results are essentially exact, but the value of $[\eta]$ has not changed much from the $d/L_c \to 0^+$ limit. This is the region in which we have tried to run all the simulations: d/L_c high enough to give good particle shape resolution, but not high enough so that ϕ is out of the linear regime. Obviously, for higher aspect ratio particles, it is harder to stay in this range of d/L_c.

Now consider the results for $[\sigma]_\infty$ shown in Fig. 2.6. The comparison between exact formula and numerical (finite element) results is similar, except that the numerical results are consistently about 5–8% above the exact curve. This error is possibly larger for larger aspect ratio particles.

Judging by the results for spheres shown in Fig. 2.6, we can expect that both the numerically computed intrinsic conductivity and viscosity will be systemically high, with the ratio $[\eta]/[\sigma]_\infty$ probably somewhat low, as the intrinsic conductivity seems to overshoot the true result slightly more than

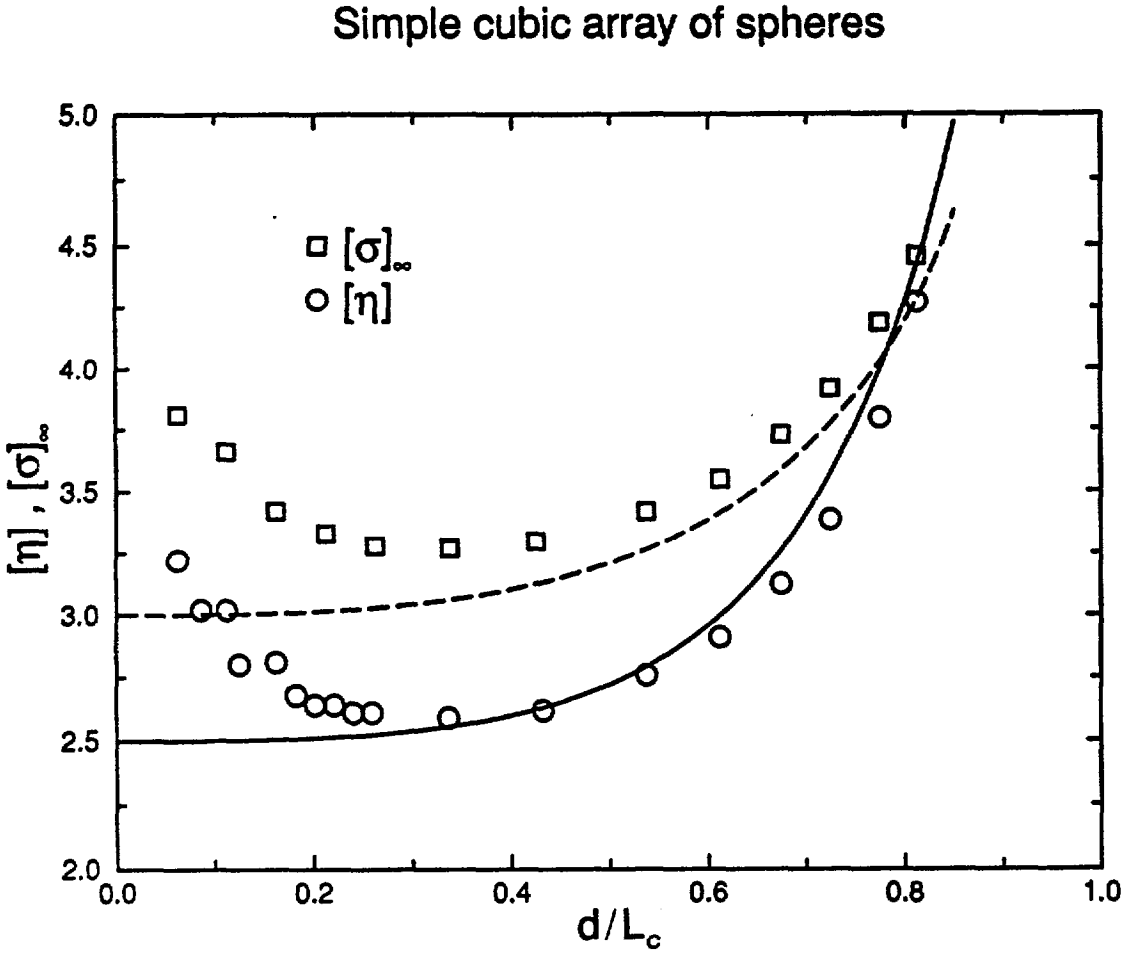

Figure 2.6. Numerical and analytical results for the intrinsic conductivity $[\sigma]_\infty$ and intrinsic viscosity $[\eta]$ for simple cubic arrays of spheres (superconducting and rigid) as a function of d/L_c, the ratio of the sphere diameter d to the sphere center spacing L_c. The length L is also defined as the size of the computational cell.

the intrinsic viscosity. Slightly increasing all the ratios involving a numerical computation of $[\sigma]_\infty$ in Tables IX–XI would improve the agreement with Eq. (3.16).

We have run other tests on the intrinsic viscosity using nonspherical shapes. Having exact results for nontrivial shapes is crucial in order to check the accuracy of numerical simulations. We computed $[\eta]$ for a spherical dumbbell with $r_p = 1.526$, giving $[\eta] \approx 4.9$, as compared to the exact value $[\eta] = 4.89$ ($r_p = 1.543$). An ellipsoid of revolution with an aspect ratio of 3 gave $[\eta] = 3.91$, which is 6.1% higher than the exact value of 3.685. The numerical result for two touching spheres was 3.62, about 5% larger than the exact result of $[\eta] = 3.45$ given in Eq. (3.13).

The important physical example of a right circular cylinder is considered next. Very precise analytical calculations of the polarizability α_e have

TABLE IX
Intrinsic Viscosity and Intrinsic Conductivity for Cylinders

Dimensions	Exact $[\sigma]_\infty$	Numerical $[\sigma]_\infty$	Numerical $[\eta]$	Numerical $\frac{[\eta]}{[\sigma]_\infty}$ Exact	Numerical $\frac{[\eta]}{[\sigma]_\infty}$ Numerical
$1 \times \frac{1}{2}$	4.106	4.32	3.45	0.84	0.80
1×1	3.401	3.56	2.90	0.85	0.81
1×2	3.622	3.79	3.08	0.85	0.81
1×4	4.704	4.93	3.93	0.84	0.80

TABLE X
Intrinsic Viscosity and Intrinsic Conductivity for Rectangular Parallelipipeds with Two Equal Edges

Aspect Ratio $(x, 1/x)$	Prolate $[\sigma]_\infty$	Prolate $[\eta]$	Prolate $[\eta]/[\sigma]_\infty$	Oblate $[\sigma]_\infty$	Oblate $[\eta]$	Oblate $[\eta]/[\sigma]_\infty$
1	3.72	3.05	0.82	3.72	3.05	0.82
2	4.22	3.41	0.81	4.15	3.36	0.81
3	5.21	4.13	0.79	4.84	3.88	0.80
4	6.38	4.98	0.78	5.58	4.44	0.80
5	7.72	5.96	0.77	6.34	5.02	0.79
10	16.4	12.3	0.75	10.2	7.92	0.78
∞				$1.11a^{3(a}$	$0.85a^{3(a}$	0.77

[a] Number density units.

TABLE XI
Intrinsic Viscosity and Intrinsic Conductivity for Various Shapes in Three Dimensions

Shape	m	$[\sigma]_\infty$	$[\eta]$	$[\eta]/[\sigma]_\infty$
Sponge	15/27	8.74	7.16	0.82
Sponge	21/27	27.1	22.0	0.81
Sponge	23/27	55.0	44.7	0.81
Sponge	25/27	192	156	0.81
Sponge	33/35	311	255	0.82
Dice ($r_p = 2.0$)		7.44	5.84	0.78
Jack		4.50	3.68	0.82
Square Ring	23/25	127	98.7	0.77
Square hollow tube	5/6	16.7	13.3	0.80

been made for the cylinder [122a and b]. Values of $[\sigma]_\infty$ calculated from these results are given in Table IX. Finite element calculations of $[\eta]$ and $[\sigma]_\infty$ for several aspect ratios, which have comparable accuracy to the sphere and touching sphere test cases, are also given in Table IX. The ratio $[\eta]/[\sigma]_\infty$ obtained from this combination of numerical and analytical calculations accords rather well with Eq. (3.16) and the general correlation Eq. (3.23). Note the difference between the columns marked Numerical/Exact and Numerical/Numerical giving the results for the ratio $[\eta]/[\sigma]_\infty$. (The term *numerical* refers to an estimate obtained by finite element calculation while *exact* refers to analytic results. The exact results often involve a nontrivial numerical evaluation of the integral expressions that define the analytic results, however.) Using the finite element estimates for the intrinsic conductivity instead of the exact results gave a value somewhat closer to the prediction of Eq. (3.16), since similar systematic computational errors for $[\eta]$ and $[\sigma]_\infty$ probably compensate.

Next, we examine the case of rectangular parallelepipeds which is summarized in Table X. Simulation results closely parallel the exact analytical calculations for the ellipsoid of revolution case discussed in Section III. Again the ratio $[\eta]/[\sigma]_\infty$ is shown to be nearly invariant with respect to shape. The oblate result for a very large aspect ratio (marked ∞ in Table X) corresponds to the case of a square plate and such objects are discussed more fully in Section VI. The value for $[\sigma]_\infty$ is approximately 7% higher than the best known experimental value (see Section VI) and we expect that our estimate of $[\eta]$ is too large by about the same amount. The $[\eta]/[\sigma]_\infty$ ratio tends to decrease as the aspect ratio increases. These results parallel the analytic results for ellipsoids of revolution in the prolate and oblate limits.

Next, we illustrate a simple means to increase $[\eta]$ and $[\sigma]_\infty$ to large values without making a very extended or flat object. We consider a cube of unit edge length, in which a square *channel* is cut through the center of each face, which passes completely through the cube. A picture of one such object is shown in Fig. 2.7a. The parameter m is taken to be the edge length of the cutout face in units of the cube edge length. We obtain a rigid cubic wire frame when m approaches 1. Notice that cutting out the center, which makes the particle more spongelike, has a very large effect on $[\eta]$ and $[\sigma]_\infty$, as seen in Table XI. It would be interesting to push the effect to the extreme in a different way by generating a Menger sponge [123] *fractal* by a repeated decimation of the cube at different scales so that $[\eta]$ and $[\sigma]_\infty$ would diverge in a characteristic fashion related to the fractal dimension of the sponge. The memory capacity of the computer was not large enough to allow us to consider more than one or two

generations of such an iteratively constructed *diffuse* object, so we presently confine ourselves to the first generation wire frame structure shown in Fig. 2.7a. The rapid increase of $[\eta]$ and $[\sigma]_\infty$ when large holes are cut out is noted. In the limit where m goes to one the intrinsic conductivity and viscosity appear to scale roughly quadratically in $(1-m)$.

In a similar vein we also consider a flat square "ring" where the length of each side is 25 and $m = 23/25$. The effect on the virials is large, as in the "sponge" case (see Table XI). Results for a square cross-section tube of width one third of the side length are given in Table XI where m of the square face equals 5/6. In this case a less pronounced effect is found.

We consider other strategies of particle modification in Table XI. For example, instead of decimating the structure we introduce protuberances onto our object. Specifically, we poke three rectangular parallelipipeds orthogonally through a sphere (see Fig. 2.7b) to create a "jack-like"

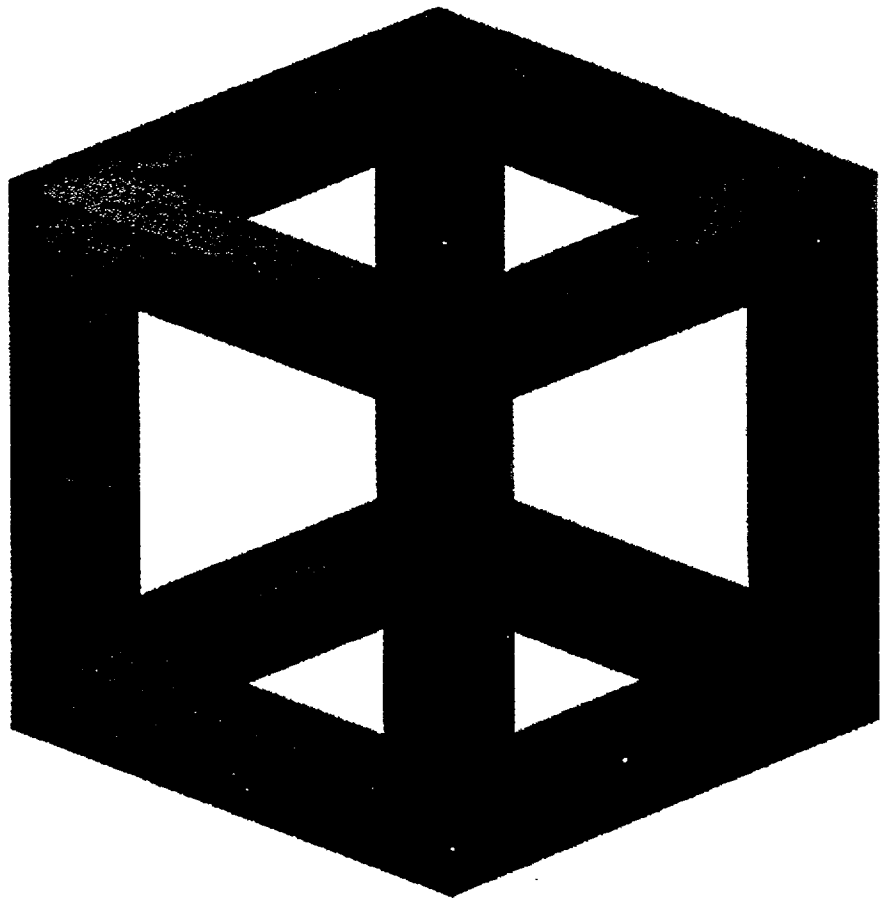

a

Figure 2.7. Model irregularly shaped objects considered by finite element computations. (a) sponge ($m = 0.6$), (b) jack-like object, and (c) dice.

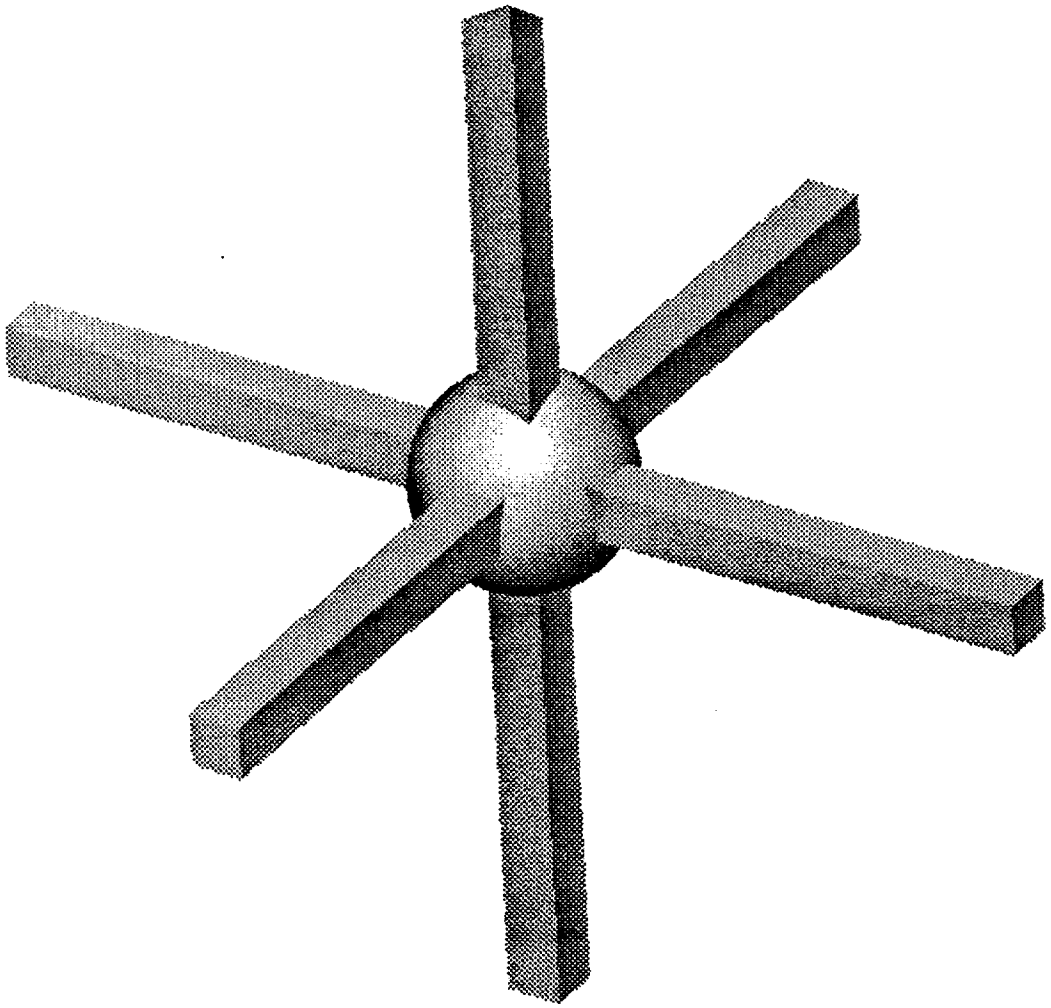

b

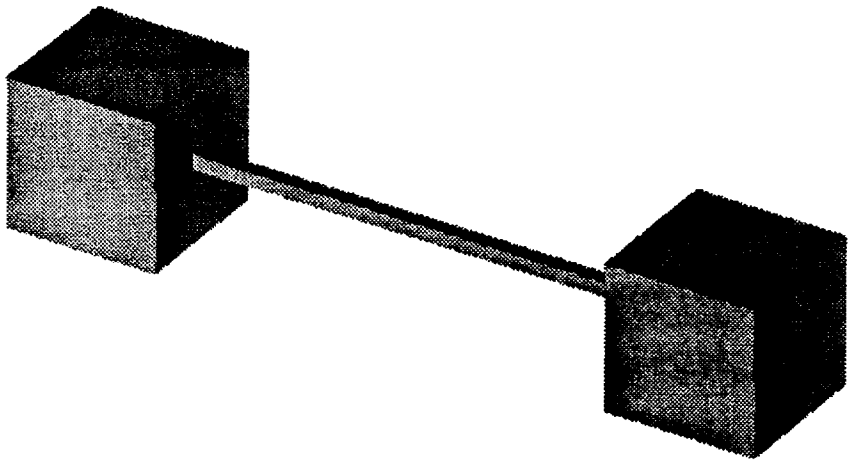

c

Figure 2.7. (*Continued*)

structure. Taking the width of these parallelipipeds as a unit of length, we take their length as 15 units and the sphere diameter as 9. The increase of $[\eta]$ and $[\sigma]_\infty$ is not as dramatic as the "sponge" case, but the effect is still appreciable. We next consider the case of separated and aligned cubes (dice), connected by a rigid, conducting wire of vanishing thickness to maintain object connectivity (see Fig. 2.7c). The results in Table XI show that such a tethering of *bulky* groups has a very large effect on the values of $[\eta]$ and $[\sigma]_\infty$. The values of $[\eta]$ for dice are similar to $[\eta]$ values for the spherical particle dumbbell (see Table VII) at comparable separations r_p.

V. INTRINSIC VISCOSITY AND CONDUCTIVITY IN d = 2

Calculation of the virial coefficients $[\eta]$, $[\sigma]_\infty$, $[\sigma]_0$, and $\langle M \rangle$ for a circle reveals a remarkable degeneracy in $d = 2$

$$[\eta] = [\sigma]_\infty = -[\sigma]_0 = \langle M \rangle / A = 2 \tag{5.1a}$$

where A is the circle area. We also have corresponding elastostatic results for hard and soft circular inclusions, $[G(\text{hard})] = -[G(\text{soft})] = 2$. The equality $[\sigma]_\infty = -[\sigma]_0$ in Eq. (5.1a) follows from the Keller–Mendelson inversion theorem [78]. Note that this relation holds for regions of *arbitrary* shape. The intrinsic viscosity result in Eq. (5.1a) is due to Brady [113] who found $[\eta] = (d+2)/2$ for hyperspheres. It is easy to show that $[\sigma]_0$ and $[\sigma]_\infty$ for hyperspheres equal

$$[\sigma]_0 = -d/(d-1), \qquad [\sigma]_\infty = d, \qquad d \geq 2 \tag{5.1b}$$

so that the equality in $d = 2$ is evidently a rather special occurrence. This can be seen in Fig. 2.8, where $-[\sigma]_0$ and $[\sigma]_\infty$ are plotted versus dimensionality d. The relation $\langle M \rangle / A = -[\sigma]_0$ follows from the Keller–Kelvin relation [Eq. (2.6)], which is not restricted to $d = 2$ and holds for regions of arbitrary shape. We note that $[\eta] \approx 2$ actually has been measured in a quasi-two-dimensional film [124].

For objects of noncircular shape the degeneracy of these shape functionals reveals itself in the general relations

$$[\sigma]_\infty = -[\sigma]_0 = \langle M \rangle / A \tag{5.2}$$

and, moreover, Eq. (3.11) implies the approximation

$$[\sigma]_\infty \approx [\eta] \tag{5.3a}$$

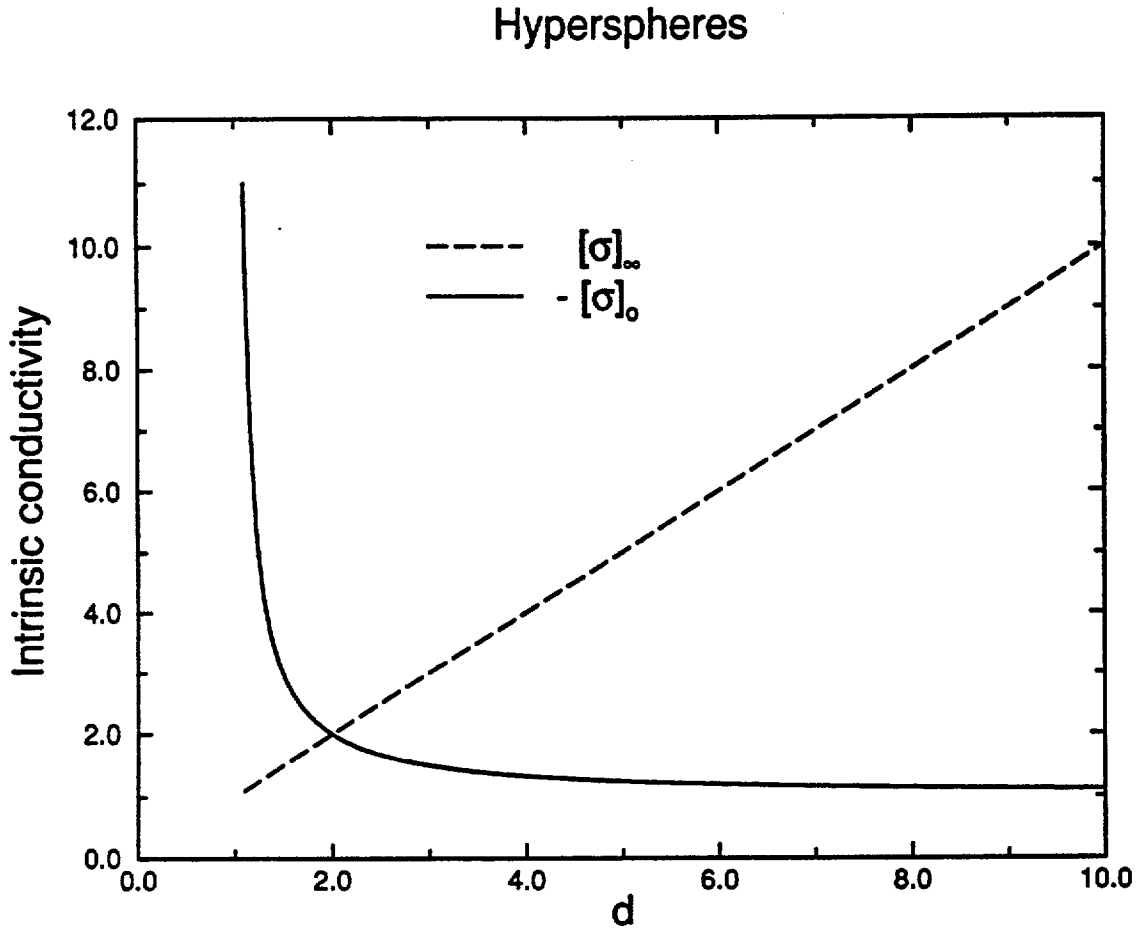

Figure 2.8. Intrinsic conductivities, $[\sigma]_0$ and $[\sigma]_\infty$, of a d-dimensional hypersphere versus dimensionality d.

In Appendix F we show that Eq. (5.3a) is *exact* for ellipses. The dependence of $[\sigma]_\infty$ and $[\eta]$ on aspect ratio x = (semi-majoraxis)/(semi-minor axis) is given by

$$[\sigma]_\infty = [\eta] = (1+x)^2/(2x) \tag{5.3b}$$

It seems entirely possible that the chain of particle property equalities in Eq. (5.1) could be exact for objects having *arbitrary* shape in $d=2$. In this section we further examine the conjecture [Eq. (5.3a)] numerically for other shapes. General agreement is found, within numerical error, in accord with our conjecture. We also provide many new, exact results for $[\sigma]_0$, $[\sigma]_\infty$, and $\langle M\rangle/A$ that derive from the recognition of the chain of equalities [Eq. (5.2)] discussed above.

Pólya [28] proved rigorously that $\langle M\rangle/A$ is minimized for circular

regions of all regions having finite area. Recognition of Eq. (5.2) then implies the physical result

$$[\sigma]_\infty = -[\sigma]_0 = \langle M \rangle / A \geq 2 \tag{5.4}$$

with equality obtained *uniquely* for the circular region. Pólya, in fact, proved much more in the process of deriving this fundamental isoperimetric inequality. He showed that $\langle M \rangle / A$ is given *exactly* by

$$\langle M \rangle / A = 2A_c/A, \qquad A_c = \pi C_L^2 \tag{5.5}$$

for regions having arbitrary shape, where C_L is variously termed the "transfinite diameter", "outer radius", or "logarithmic capacity", and A_c is defined here as the conformal area. (The area A and perimeter P of regions having general shape [30b] satisfy the important isoperimetric inequalities $A \leq A_c$, $P \geq 2\pi C_L$, and we note that $P \approx 2\pi C_L$ is often a reasonable approximation for objects having a modest shape irregularity [26].)

The transfinite diameter C_L is a basic measure of the average *size* of a bounded plane set, and can be defined in a variety of equivalent ways [29,30]. The parameter C_L, for example, is defined as the conformally invariant magnitude of Dirichlet's integral associated with the exterior of the region defining the particle [29]. The equivalent transfinite diameter can be expressed in terms of the Euclidean metric defining the distance between points in the set [30]. Perhaps the most useful definition of C_L involves the purely geometrical construction of mapping the exterior of a region Ω having an arbitrary but simply connected shape and finite area onto a circular region in such a fashion that the points at a large distance from Ω are asymptotically unaffected by the transformation [28]. The radius of this uniquely defined transformed circular region equals C_L. This transformation is basically the content of the Riemann mapping theorem [30c]. The origin of the outer radius terminology is thus apparent.

The invariance of C_L under conformal transformations is very convenient in the numerical computation of C_L and thus $[\sigma]_\infty$ and the other shape functionals of physical interest. It would be useful to have a program to calculate C_L for any conceivable bounded (compact) plane set, so that the physical consequences of shape variations could be explained easily. In Fig. 2.9 we indicate the results [125,126] obtained using "state of the art" conformal transformation methodology. The intrinsic conductivities of regions a) and b) in Fig. 2.9 were calculated using the energy integral definition of logarithmic capacity (see [29]) for certain spiral shaped lines

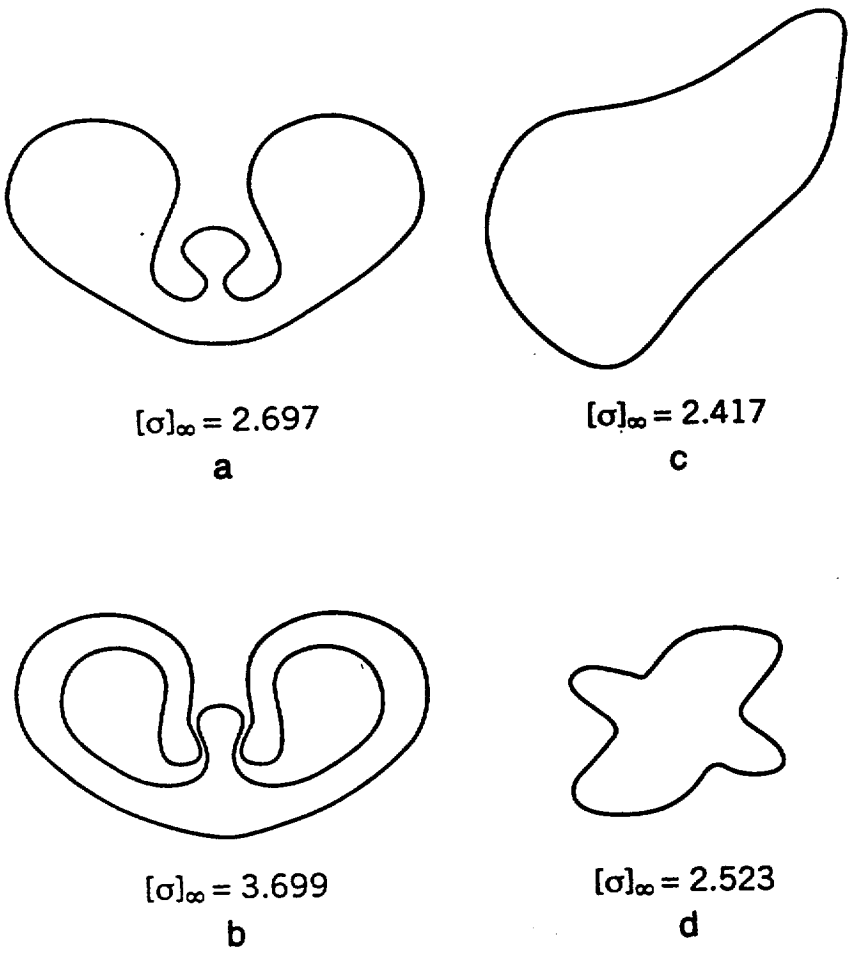

Figure 2.9. Various closed regions and numerical conformal mapping calculations for $[\sigma]_\infty$ corresponding to these regions. Numerical calculations were performed for us by McFadden [126].

that were then mapped conformally onto the indicated regions. By virtue of the invariance of C_L under comformal transformation, the C_L values for the original linear curves (not shown) equals C_L for the indicated regions in Fig. 2.9 and accurate estimates of C_L are obtained in this fashion. Any smooth nonintersecting curve in the plane can be mapped to its corresponding closed region in this fashion so that a large class of C_L calculations becomes possible for rather intricately shaped regions. Note the large value of $[\sigma]_\infty$ in Fig. 2.9c that results from the screening of the interior of the region in much the same fashion as the *sponge* shaped objects discused in the previous section. In c and d of Fig. 2.9 an alternative method of calculating C_L by conformally mapping the indicated regions onto a circular region of radius C_L numerically [126] is illustrated. This method is powerful, provided the region does not have

sharp corners. (Other methods exist for polygonally shaped boundaries that are amenable to full analytic treatment and some of these results are discussed below.) We conclude that although many regions can be treated by these conformal techniques, there is still no simple and general method that can be adapted to calculate C_L for arbitrarily shaped regions. This remains an important mathematical challenge.

We mention that McKean [80c] summarized a formal algorithm for calculating C_L that has the generality we seek. This method involves hitting the 2D domains with random walks. This approach is similar to the technique implemented recently [80a and b] to calculate the Newtonian capacity [see Eq. (3.10)] in $d = 3$. Implementation of this algorithm should allow the numerical calculation of C_L for any bounded plane set.

Since C_L is a central object in the harmonic analysis of two dimensions [26, 28–30], there exist extensive tabulations of C_L [26, 29]. We may combine this information with Eq. (5.5) to obtain numerous *exact* results for the intrinsic conductivity. Table XII gives a sampling of some of these results. Further tabulation of expressions for C_L are given by Pólya and Szegö [26] and Landkof [29].

Pólya's isoperimetric inequality, $[\sigma]_\infty \geq 2$ [see Eq. (5.4)], is illustrated nicely by the case of the symmetric n-gon. Table XIII shows results for $[\sigma]_\infty$ as a function of n. The circle result is recovered in the limit $n \to \infty$.

TABLE XII

Logarithmic Capacity C_L Formulas for Variously Shaped Regions in Two Dimensions.

Region type	Logarithmic Capacity C_L	Intrinsic Conductivity $[\sigma]_\infty$
1. Circle of radius a	a	2
2. Ellipse, Axes of length a and b	$(a+b)/2$	$(a+b)^2/2ab$
3. Square of side length a	$\dfrac{\Gamma^2(\frac{1}{4})a}{4\pi^{3/2}} \approx 0.59017a$	2.1884
4. Triangles:		
(a) Equilateral triangle, Height h	$\dfrac{\Gamma^3(\frac{1}{3})h}{4\pi^2} \approx 0.4870h$	2.5809
(b) Right triangle, Long side of length h	$(5^{5/12}\Gamma^3(\frac{1}{3})/10^{10/3}\pi^2)h \approx 0.37791h$	3.1090
(c) Isosceles right triangle, Long side of length h	$\dfrac{3^{3/4}\Gamma^2(\frac{1}{4})a}{4(2\pi)^{3/2}} \approx 0.47563h$	2.8431
5. Hexagon of side length a	$[3\Gamma^3(\frac{1}{3})/2^{8/3}\pi^2]a \approx 0.92032a$	2.0486
6. Symmetric n-gon, Side length a	$[n\Gamma(1+1/n)/2^{1+2/n}\sqrt{\pi}\Gamma(\frac{1}{2}+1/n)]a$	$[\tan(\pi/n)/2\pi n]\Gamma^4(1/n)/\Gamma^2(2/n)$
7. Semicircle of radius a	$(4/3^{3/2})a$	$(\frac{4}{3})^3 = 2.3704$

TABLE XIII
Intrinsic Conductivity for Regular n-gons in Two Dimensions

Shape	n	$[\sigma]_\infty$
Triangle	3	$2.5811\cdots$
Square	4	$2.1884\cdots$
Pentagon	5	$2.0878\cdots$
Hexagon	6	$2.0486\cdots$
Octagon	8	$2.0197\cdots$
Circle	∞	2

This beautiful result and others in Table XIII were recently rediscovered by Thorpe [127]. The domain fuctional $[\sigma]_\infty$ for n-gons tends to increase as the symmetry of the n-gon [26] is reduced by shape deformation. For example, the intrinsic conductivity of the equilateral triangle and the square are minimal for all triangles and quadrilaterals, respectively [26,128]. *A* systematic investigation of the variation of $[\sigma]_\infty$ with symmetry would be interesting, since ample evidence indicates that $[\sigma]_\infty$ is smaller for regions of higher symmetry.

Results for C_L and $[\sigma]_\infty$ are also given for linelike regions in Table XII. Such resuls are special to $d=2$ since it is well known that the *Newtonian capacity* C [see Eq. (3.10)] vanishes for any finite length differentiable curve [129] in $d=3$. Thus, we can expect $[\sigma]_\infty$ and $[\eta]$, as well as the friction coefficient of any smooth curve in $d=3$, to equal zero. The finiteness for the capacity of Brownian paths [130] in three dimensions owes itself to the fact that such curves are *typically* nondifferentiable and this property of Brownian paths has numerous implications for polymer physics and phase transition theory.

We next turn to a test of the prediction Eq. (3.11), relating $[\eta]$ and $[\sigma]_\infty$ for nonelliptical shaped regions. Finite element calculations of $[\eta]$ for objects of various shapes are indicated in Table XIV. Our numerical estimate for a circle is $[\eta]=1.96$, which is 2% *lower* than the exact value. Checks against the exact result [Eq. (5.3a)] for ellipses show that the finite element computations of $[\eta]$ in $d=2$ tend to be slightly *lower* than the exact values, in contrast to the numerical calculations in $d=3$, which tend to be slighly *higher* than the exact values. For example, the result for $[\eta]$ for an ellipse of aspect ratio $101/21=4.81$ is 3.33, 5.1% lower than predicted by Eq. (5.3b).

Exact calculations of **M** for many interesting shapes are available in the hydrodynamic literature because of important aerodynamic and ship dynamics applications [63, 69–71] and we include the corresponding exact $[\sigma]_\infty$ and numerical $[\eta]$ results for a parabolic lens, spherical lens,

TABLE XIV
Intrinsic Viscosity and Intrinsic Conductivity for Various Shapes in Two Dimensions

Shape	Aspect Ratio	$[\sigma]_\infty$	$[\eta]$	$[\eta]/[\sigma]_\infty$
Rectangle	1	2.19	2.15	0.98
	2	2.40	2.33	0.97
	3	2.76	2.65	0.96
	4	3.15	3.01	0.96
	5	3.55	3.37	0.95
	8	4.76	4.51	0.95
	12	6.38	6.03	0.95
	14	7.18	6.78	0.94
	16	7.99	7.52	0.94
	18	8.79	8.25	0.94
	19	9.20	8.64	0.94
	20	9.60	8.94	0.93
Parabolic lens		2.287	2.21	0.97
Spherical lens		3.236	3.19	0.99
Two touching circles	$r_p = 1$	$\pi^2/4$	2.38	0.96

touching circles, and a rectangle of varying aspect ratio x in Table XIV. Thorpe [127] gives a recent discussion of $[\sigma]_\infty$ for the rectangle. We also mention calculations of $\langle M \rangle / A$ and thus $[\sigma]_\infty$ for the exotic starlike hypocycloid and teardrop-like shapes calculated by Wrinch [70], which are difficult to approximate by finite element methods and even the numerical conformal mapping methods. These examples provide a good challenge for any numerical method for calculating C_L.

Looking more closely at the results for the $[\eta]/[\sigma]_\infty$ ratio for rectangles in Table XIV, we see that for the square this ratio is about 2% less than 1. The error in $[\eta]$ for the square should be comparable to that for the circle and so the actual value of this ratio could easily be one—allowing for a 2% error on the low side for the intrinsic viscosity as in the circle case. Consider now the rectangle with an aspect ratio of 5. If the error in the intrinsic viscosity is similar to that of the ellipse with an aspect ratio of 5, then this value should be about 5% lower, which would make the true value of the ratio 1. Higher resolution should improve the computation, if indeed the deviation from Eq. (5.3a) is only due to finite resolution error. To test this, we recomputed the intrinsic viscosity for a rectangle of aspect ratio 5 using approximately double the resolution (consuming 45 h of supercomputer time). The ratio in Table XIV changed from 0.95 to 0.97, as expected. Also, the error in the intrinsic viscosity is expected to gradually increase with the aspect ratio at a given resolution, as described

above for the $d = 3$ case. Considering this finite resolution error, the ratio of the intrinsic conductivity and viscosity for rectangles is consistent with Eq. (5.3a) being *exact*. Results for the other shapes listed in Table XIV are also consistent with this error analysis and Eq. (5.3a). We also recall that Eq. (5.3a) is exact in the case of an ellipse [see Eq. (5.3b)], so on the basis of this analytical and numerical evidence we conjecture that $[\eta] = [\sigma]_\infty$ in $d = 2$.

VI. INTRINSIC VISCOSITY AND THE POLARIZABILITY OF PLATES

Plates occupy an intermediate position between objects extended three dimensionally and objects in three dimensions that can be confined to a plane. The loss of the extension of the body in the dimension normal to the object plane has the effect of decreasing the number of nonzero tensor components for $\boldsymbol{\alpha}_e$ and $\boldsymbol{\alpha}_m$. We noticed in Section II that the tensor components for nearly flat tend to exhibit rapid variation when the thickness is varied. This makes such object shapes useful for effectively modifying the properties of a medium.

The polarization tensors of plates are crucial in the description of long wavelength scattering of electromagnetic and pressure waves through apertures [88–91]. This connection was apparently first noticed by Rayleigh [81a], but the practical significance of this connection was appreciated more recently because of the difficulty of calculations of the polarization tensor components for plates having general shapes. The magnetic polarizability $\boldsymbol{\alpha}_m$ (or the mathematical equivalent $\mathbf{M}$) is also important in the description of the flow of viscous fluid through screens [131]. The technological literature is a good source of results regarding the polarizability of plate-like regions.

The theoretical impetus for calculating the polarizability tensors of plates came from the needs of a developing microwave technology [47–50]. Bethe [88a] calculated the magnetic and electric polarizability of circular plates in his classical theory of the diffraction of electromagnetic radiation by a hole small compared with the incident wavelength and later [89b] he gave results for elliptic plates. Cohn [49, 132] made electrolytic-tank measurements of the polarizability components of plates of numerous shapes (rectangular slots, rounded slots, rosettes, dumbbells, crossed slots, etc.) to provide this important technological information. The electric polarizability of an aperture of general shape was measured by simply cutting out a nonconducting material of the given shape and suspending the object with thin nonconducting wires in an electrolytic solution between two electrodes coplanar with the inclusion. Similarly,

the magnetic polarization was measured by suspending a metallic inclusion normal to the electrode surfaces [132]. These experimental measurements of the electric and magnetic polarizability of plates have had many important applications.

Recently, numerical solutions of integral equations defining the electric and magnetic polarizability tensors have been obtained for a wide variety of shapes [72, 73]. These calculations have confirmed the accuracy of Cohn's measurements and a general correlation of the magnetic and electrical aperture polarizations have been obtained for certain families of objects [72, 73]. Significant progress has recently been made by Fabrikant [75] who developed an *analytical* technique for calculating the magnetic and electric polarizability tensors of plates that compares very well with previous numerical and experimental results. Fabrikant treats polygons, rectangles, the rhombus, a circular sector, and other shapes, and the method can apparently be applied to regions having very general shapes.

The utilization of these important theoretical developments requires the recognition of the relation between *aperture polarizabilities* $\boldsymbol{\alpha}_e$(apert.) and $\boldsymbol{\alpha}_m$(apert.), used in the technical literature, and the ordinary polarizabilities, $\boldsymbol{\alpha}_e$ and $\boldsymbol{\alpha}_m$, discussed above. Babinet's principle [73,89] implies that these quantities are related by the definitions

$$\boldsymbol{\alpha}_e(\text{apert.}) = -\boldsymbol{\alpha}_m/4, \qquad \boldsymbol{\alpha}_m(\text{apert.}) = \boldsymbol{\alpha}_e/4 \tag{6.1}$$

Simple physical considerations show that $\boldsymbol{\alpha}_m$ for a flat plate is effectively a scalar, having only one nonzero component. Correspondingly, the component of $\boldsymbol{\alpha}_e$ for a metal plate normal to an applied field vanishes, since there is no way to separate charges in this case. However, there are nonvanishing components to $\boldsymbol{\alpha}_e$ when the plate is aligned along the field direction. From these observations we immediately obtain numerous results for $\boldsymbol{\alpha}_e$ and $\boldsymbol{\alpha}_m$ from the literature of electromagnetic and sound scattering through apertures.

For example, we can obtain the magnetic polarizability of an elliptic plate from Bethe's formula for the electric aperture polarizability of an ellipse (plate is normal to field direction)

$$\alpha_m(T) = (4\pi ab^2/3)/E(e) \tag{6.2}$$

where a and b are semimajor and semiminor axes, e is the eccentricity, $e = [1-(b/a)^2]^{1/2}$, and E is a complete elliptic function of the second kind (T and L denote the transverse and longitudinal components of the polarizability tensor as defined in Sect. 3). The average $\langle \alpha_m \rangle$ of a plate generally equals

$$\langle \alpha_m \rangle = \tfrac{1}{3}\alpha_m(T) \tag{6.3}$$

since there is only one nonzero component, as mentioned above. Note that Eqs. (6.2) and (6.3) reduce to Eq. (3.17) for the circular disk. Numerous other examples follow along these lines from recent numerical calculations [72, 73] and analytical calculations by Fabrikant [75].

Results for the electric polarizability can be similarly obtained, although these results tend to have a more complicated mathematical description. We mention the important experimental estimate [49] of $\alpha_e(L)$ for a square plate having a side length a,

$$\alpha_e(L) = 1.02a^3 \text{ (expt.)} \tag{6.4}$$

placed parallel to the applied field. There are two components of the electric polarizability for an asymmetric rectangular plate, of course. The estimate Eq. (6.4) was obtained from Cohn's electrolytic tank measurements and this value has been confirmed by more recent numerical [72, 73] and analytical studies [75] to an accuracy on the order of 1%. Our finite element technique gives $\alpha_e(L) = 1.09a^3$ for the square plate, which is apparently too high by the usual 5–6% in $d = 3$. This result is listed in Table X.

These quantitative estimates of $\boldsymbol{\alpha}_e$ and $\boldsymbol{\alpha}_m$ for plates from this variety of sources is very useful in combination with the approximate invariant relation [Eq. (3.16)]. In Section III we mentioned the exact result

$$[\eta] = \tfrac{4}{5}[\sigma]_\infty \tag{6.5}$$

for circular plates. Combination of the extensive plate estimates with Eq. (6.5) then yields predictions for $[\eta]$ that can be checked against experiment. Further efforts are needed on the difficult problem of analytically calculating $[\eta]$ for arbitrarily shaped plate-like regions, which certainly is not going to be any more tractable than the electrostatic and magnetostatic analogs. We note that our finite element technique could be used to estimate the polarizabilities, intrinsic conductivity, and intrinsic viscosity of arbitrarily shaped objects, and that the method is not limited to large values of the relative conductivity Δ_σ. The numerical calculations are actually *faster and more accurate* when Δ_σ is not large.

VII. CONCLUSIONS AND SUMMARY

There are many physical processes for which the solution of the Laplace equation on the exterior of a body of general shape is central to the theoretical description. Previous papers [80] discussed the exterior Dirich-

let problem for the Laplace equation and the calculation of the capacity C, which is the shape functional associated with this problem. This chapter discusses other functionals of shape associated with the solution of the Laplace and the Navier–Stokes equations on the exterior of objects having general shape. These functionals [26] include the electric and magnetic polarizabilities, the hydrodynamic virtual mass, and the intrinsic viscosity.

New numerical and analytical results for these shape functionals, along with values from a large literature, were obtained to check a proposed relation between shape functionals associated with the Laplace equation, namely, the electric polarizability and a shape functional associated with the Navier–Stokes equation, the intrinsic viscosity. Our new approximate relation is a natural generalization of a result of Hubbard and Douglas [27] approximately relating the translational friction coefficient (Navier–Stokes equation) to the electrostatic capacity (Laplace equation). These relations between hydrodynamic theory and electromagnetic theory complement the classical relation between the *effective mass* **M** of *perfect* fluids and the magnetic polarizability $\boldsymbol{\alpha}_m$ observed by Keller et al. and Kelvin [57,58].

Exact and numerical results confirm that the intrinsic viscosity $[\eta]$ is proportional to the intrinsic conductivity $[\sigma]_\infty$ of conducting particles of arbitrary shape to within about a 5% approximation,

$$[\eta] \approx (0.79 \pm 0.04)[\sigma]_\infty \tag{7.1a}$$

in three dimensions. In two dimensions we find $[\eta]$ exactly equals $[\sigma]_\infty$ for ellipses. Data for other shapes, allowing for a usual underestimation of $[\eta]$ by 2–5% in our $d = 2$ finite element method, are in general agreement with this conjectured approximation. On the basis of this evidence, we conjecture that $[\eta] = [\sigma]_\infty$ for all shapes in $d = 2$. Further exact calcuations of $[\eta]$ for some of the shapes discussed would be useful in developing a proof (or disproof) of this conjecture. All of our findings agree well with the predictions of our angular averaging approximation

$$[\eta] \approx [(d+2)/(2d)][\sigma]_\infty \tag{7.2a}$$

$$[\eta] \approx 0.83[\sigma]_\infty, \qquad d = 3 \tag{7.2b}$$

$$[\eta] \approx [\sigma]_\infty, \qquad d = 2 \tag{7.2c}$$

Although our primary goal in this chapter was to test relation (7.2), the tabulated values of $[\sigma]_\infty$, $[\sigma]_0$, and $[\eta]$ for numerous shapes and the discussion of the general shape parameters that affect these quantities

should find wide application. Inevitably, this information becomes important when we attempt to resume the virial expansions, such as Eq. (2.1), to provide a useful description of suspensions of arbitrarily shaped particles in a matrix at high concentrations.

APPENDIX A
VIRTUAL MASS AND THE ACOUSTIC INDEX OF REFRACTION

It seems likely that the fundamental relation [Eq. (2.6)] was recognized much earlier since the mathematical equivalence between the flow of inviscid fluids and electrical conduction is well known [58,64,102]. Recently, Brown [133a] pointed out a nonperturbative generalization of Eq. (2.6). He showed that the conductivity σ of a nonconducting rigid matrix filled with a conducting fluid of conductivity σ_0 is related to the change in the average *effective mass* (effective fluid density) of the corresponding inviscid fluid at arbitrary volume fractions. Johnson and Sen [134] showed that this analogy also implies that the acoustic index of refraction n of an ideal fluid in a rigid matrix equals

$$n^2 = (1-\phi)(\sigma_0/\sigma) \tag{A.1}$$

where $1-\phi$ is the *porosity*. This relation, like so many others, was apparently known to Rayleigh [135]. Acoustic index of refraction measurements (fourth sound) for superfluid He^4 in a porous medium [136] and salt water in a sintered glass bead pack [24d] confirm Eq. (A.1) to a good approximation. Recently, there has been a nonperturbative generalization of Eq. (2.2a) [137]

$$\sigma/\sigma_0 = (1-\phi)/t_E \tag{A.2}$$

where the *electrical tortuosity* α_E is defined as $t_E = D_0/D_p$, where D_p is the diffusion coefficient of particles in the fluid region such that the diffusing particles obey a *reflecting* boundary condition when they encounter the matrix. The parameter D_0 is the diffusion coefficient of the particle in the fluid in the absence of the rigid matrix.

The diffusion coefficient observed in a macroscopic diffusion measurement on a porous medium with insulating rigid inclusions, however, is *not equal* to the pore diffusion coefficient, D_p. Rather, the diffusion coefficient D measured in a macroscopic measurement is related to D_p as

$$D = D_p/(1-\phi) \tag{A.3}$$

so that Eq. (A.2) reduces to the generalized Einstein relation [138].

$$\sigma/\sigma_0 = D/D_0 \tag{A.4}$$

For low concentrations ($\phi \to 0^+$) the nonperturbative relation [Eq. (A.4)] reduces to the known virial expansion [16a, 16d] for fixed hard sphere inclusions having a reflecting boundary condition

$$\sigma/\sigma_0 = D/D_0 = 1 + [\sigma]_0 + O(\phi^2), \qquad [\sigma]_0 = -\langle M \rangle / V_p \tag{A.5a}$$

$$\langle M \rangle / V_p = \tfrac{3}{2} \qquad (d = 3; \text{ sphere}) \tag{A.5b}$$

From a conductivity standpoint Eq. (A.5a) corresponds to insulating inclusions. Equation (A.5a) shows that the average effective mass $\langle M \rangle$ of the rigid inclusions determines the leading concentration dependence of the diffusion coefficient in a porous medium in the absence of particle interaction. We note that the insensitivity of $[\sigma]_0$ to particle shape for extended particles (not platelets) means that as particles aggregate at higher concentration then Eq. (A.5) should remain a good approximation. Experiment, indeed, shows that the leading linear concentration dependence in Eq. (A.5) holds to a good approximation over a wide concentration range [33, 34].

APPENDIX B
POLARIZATION FORMALISM FOR ELLIPSOIDS

Stratton [52a] defines a set of numbers A_i, which often arise in the discussion of the properties of ellipsoids. These numbers are defined by the integrals (Stratton does not include prefactor $a_1 a_2 a_3$):

$$A_i = a_1 a_2 a_3 \int_0^\infty dx[(a_i^2 + x)R(x)]^{-1} \tag{B.1}$$

where

$$R(x) = [(a_1^2 + x)(a_2^2 + x)(a_3^2 + x)]^{1/2} \tag{B.2}$$

and the constants a_1, a_2, and a_3 are the ellipsoid semiaxes lengths with $V_p = 4\pi a_1 a_2 a_3/3$. The A_i parameters obey the simple sum rule,

$$A_1 + A_2 + A_3 = 2 \tag{B.3}$$

Equation (B.3) is useful since it reduces the integrals that need to be computed for a general ellipsoid from three to two. Various combinations and ratios of these numbers are required for the intrinsic viscosity calculation and are given in Appendix C. Note that Stratton uses the notation A_i for these quantities, while Haber and Brenner [14] and

Scheraga [120a] use α_i. We followed Stratton's notation to avoid confusion with our notation for the polarizability.

The A_i integrals can be expressed as combinations of the standard elliptic integrals. However, for numerical purposes, it is just as simple to evaluate the integrals directly using Gauss–Legendre quadrature. It is first useful to transform the integrals by letting $x = \tan^2(\theta)$, so that $0 < \theta < \pi/2$. An integration mesh can be easily set up and enough points chosen to achieve convergence. For the smaller values of the ratios a_3/a_1 and a_3/a_2 (on the order of 50 or less) we needed less than 100 points in the quadrature mesh to achieve 5–6 significant figure accuracy, while for the highest values of these ratios studied (on the order 10,00) we needed 10000 points in the integration mesh to achieve the same accuracy.

For ellipsoids of revolution we have $a_1 = a_2$ so that $a_3/a_1 = a_3/a_2 = x$, the aspect ratio and the number of integrals needed reduces to 1. In this case we have $A_1 = A_2 = (2 - A_3)/2$ and A_3 is given by

$$A_3 = [x/(x^2 - 1)][B - 2/x] \tag{B.4}$$

where for prolate ellipsoids of revolution $(x > 1)$

$$B = [(x^2 - 1)]^{-1/2} \ln \{[x + (x^2 + 1)^{1/2}]/[x - (x^2 + 1)^{1/2}]\} \tag{B.5}$$

and for oblate ellipsoids of revolution $(x < 1)$

$$B = 2\cos^{-1}(x)/(x^2 - 1)^{1/2} \tag{B.6}$$

With the A_i functions defined for any ellipsoid the formulas in Stratton can be easily evaluated to compute the polarizability for any choice of matrix conductivity σ_0 and particle conductivity σ_p. For the case of a highly conducting ellipsoidal inclusion, $\sigma_p \gg \sigma_0$, the components of α_e are defined as

$$\alpha_e(i)/V_p = 2/A_i \tag{B.7}$$

In the case of an insulating ellipsoidal inclusion the components of α_m are given by

$$\alpha_m(i)/V_p = (A_i/2 - 1)^{-1} \tag{B.8}$$

and the intrinsic conductivity equals

$$[\sigma] = (\alpha_1 + \alpha_2 + \alpha_3)/3 \tag{B.9}$$

APPENDIX C
INTRINSIC VISCOSITY FORMALISM FOR ELLIPSOIDS AND OTHER SHAPES

Haber and Brenner worked out the isotropically averaged intrinsic viscosity for ellipsoidal particles [14]. This formalism is valid for any choice of the axis lengths a_1, a_2, and a_3. Values of the A_i functions are required, as well as auxiliary functions that can be defined in terms of the A_i, denoted A_i' and A_i''. They are given as follows (i, j, k are permuted cyclically):

$$A_i' = a_j a_k (A_j - A_k)/(a_k^2 - a_j^2) \tag{C.1}$$

$$A_i'' = (a_j^2 A_j - a_k^2 A_k)/(a_j^2 - a_k^2) \tag{C.2}$$

[The expression for A_i' is opposite in sign from that given in Haber and Brenner [14], and this typographical error is corrected in Eq. (C.1).] The following quantities are then formed:

$$Q_i = \tfrac{4}{5} A_i''/(A_1'' A_2'' + A_2'' A_3'' + A_1'' A_3'') \tag{C.3}$$

$$q_i = a_j a_k (A_j + A_k)/[A_i'(a_j^2 A_j + a_k^2 A_k)] \tag{C.4}$$

The intrinsic viscosity can be expressed in terms of these constants

$$[\eta] = \tfrac{2}{15}(Q_1 + Q_2 + Q_3) + \tfrac{2}{2}(q_1 + q_2 + q_3) \tag{C.5}$$

This equation is tabulated in Tables V and VI.

The intrinsic viscosity for anisotropic particles is in general a fourth rank tensor, with the same symmetries as the elastic stiffness tensor [117] for the given symmetry of the particle. For example, the intrinsic viscosity for an aligned triaxial ellipsoid is a fourth rank tensor having the same symmetry as the elastic stiffness tensor for an orthorhombic crystal [117, 139]. Formally, this can be stated using either the stress to define the effective viscosity of a single-particle suspension, or using the energy dissipation rate [14]. In the following, the discussion of Haber and Brenner is followed [14] in presenting both methods.

Consider an isolated particle, immersed at rest in a homogeneous, incompressible fluid with viscosity η_0. We restrict consideration to particles that have a center of symmetry. The traceless rate of strain field is denoted $\mathbf{S}$, such that if the particle were not there, $\mathbf{S} = \mathbf{S}_0$ would be a uniform traceless rate of strain tensor. Far away from the particle, the velocity fields must go to $\mathbf{v} = \mathbf{S}_0 \mathbf{r}$ and the average of $\mathbf{S}$ over all space,

denoted $\langle S \rangle$, equals $\mathbf{S}_0$ [14]. Solving Stokes' equations for the fluid velocity and pressure fields due to the presence of the rigid particle and then averaging the viscous stress $\boldsymbol{\sigma}_s$ over the volume of the sample gives

$$\boldsymbol{\sigma}_s = 2\eta_0 \, [\mathbf{I} + \phi \boldsymbol{\Psi}] : \mathbf{S}_0 \tag{C.6}$$

where ϕ is the volume fraction of the particles. This result is limited to a sufficiently dilute suspension so that each particle can be considered to be independent of the others. The parameter Ψ_{ijkl} is a fourth rank tensor of the same symmetry as the particle. If the calculation is carried out in a periodic array of particles, as was done in the finite element work explained in Appendix E, then Ψ_{ijkl} has whichever symmetry is lower, the particle or the array. For example, when considering a cubic array of spheres, Ψ_{ijkl} has cubic symmetry and is not isotropic like the sphere.

The isotropically averaged intrinsic viscosity that we have studied in this chapter is obtained by calculating the isotropic average $\langle \Psi_{ijkl} \rangle$, using the standard definition of rotational tensor averaging [140] and then using Eq. (3.2) to obtain

$$[\eta] = \langle \Psi_{ijkl} \rangle \tag{C.7}$$

We are operating under the assumption of "overwhelming Brownian motion" [117], so that the applied shear is weak compared to the Brownian motion of the particle, so that all orientations are equally probable. In this case, the quantity Ψ_{ijkl} is calculated when holding the particle positionally and orientationally fixed in space. The rotational average of Ψ_{ijkl} then incorporates the fact that all orientations are equally probable. The opposite case would be the strong applied shear case, where Brownian motion can be ignored, and the particle has anisotropic orientation due to the applied shear field. For an anisotropic particle this would correspond to the elastic case, since in the elastic case a rigid particle maintains its shape but can orient itself with the applied field.

Since the intrinsic viscosity tensor has the same symmetries as the equivalent elastic tensor, the averaging procedure discussed above is exactly the same as taking the Voigt average [141] of the elastic stiffness tensor for a polycrystalline sample. This procedure has been worked out for every crystal symmetry of interest and results are available in the literature. For example, all the particles considered numerically in this chapter have tetragonal or higher symmetry. Tetragonal symmetry means square symmetry in the cross-sectional plane, with the third direction being different (a rectangular parallelipiped, with $a = b \neq c$, has tetragon-

al symmetry). The angularly averaged shear modulus $\langle G \rangle$ is obtained from the elastic stiffness tensor C_{ijkl} (tetragonal symmetry) by

$$\langle G \rangle = \tfrac{1}{30}[M_G + 3C_{1111} - 3C_{1122} + 12C_{2323} + 6C_{1212})] \tag{C.8a}$$

$$M_G \equiv C_{1111} + C_{1122} + 2C_{3333} - 4C_{1133} \tag{C.8b}$$

To obtain the rotationally averaged intrinsic viscosity, simply substitute Ψ_{ijkl} for C_{ijkl}, and multiply by a factor of 2, because the elastic tensor averages are defined for a system of notation such that the shear strain is twice that used for the rate of shear strain in fluid mechanics [142,143]. One should note that in [14] and [117] a factor of $\frac{5}{2}$ is often taken out of the definition of Ψ_{ijkl} so that $\langle \Psi_{ijkl} \rangle$ is then normalized to equal 1 for a spherical particle.

The intrinsic viscosity can also be defined via the energy-dissipation rate. Since this is the way that the finite-element simulations were done and since it offers an easy way to do the averages numerically, we present this method as well. We again follow the discussion of [14].

For the same case considered above, it is found that the rotationally averaged rate of energy dissipation $\langle E \rangle$ is given by

$$\langle E \rangle = 2\eta_0[1 + [\eta]\phi]S^0_{ij}S^0_{ij} \tag{C.9}$$

For tetragonal symmetry and higher it is possible to select the terms of $\mathbf{S}_0$ so that the energy dissipation rate E [143]

$$E = \tfrac{1}{4}S^0_{ij}\eta_{ijkl}S^0_{kl} \tag{C.10}$$

gives the terms needed to form the average Eq. (C.8). One choice for S^0_{ij}, which gives the correct combination of terms for tetragonal symmetry, is the following:

$$S_{11} = [2 + \sqrt{3}]^{1/2}/\sqrt{30} \tag{C.11a}$$

$$S_{22} = -[2 - \sqrt{3}]^{1/2}/\sqrt{30} \tag{C.11b}$$

$$S_{33} = -(S_{11} + S_{22})/\sqrt{30} \tag{C.11c}$$

$$S_{13} = S_{23} = S_{12} = 1/\sqrt{5} \tag{C.11d}$$

Computing the energy for this applied rate of strain tensor gives precisely the combination of terms in Eq. (C.8). By subtracting the original energy from that found without a particle being present, the rotationally averaged intrinsic viscosity can be read off from the numerical results.

APPENDIX D
EXACT SOLUTION OF THE POLARIZATION OF A DUMBBELL

It was not previously noticed that all the mathematical apparatus necessary for computing the components of α_e for the spherical particle dumbbell had been in place since the publication of a paper by Davis [144]. The problem is the following: Take two highly conducting spheres of the same radius connected by a very thin conducting wire so that both spheres in this dumbbell are at the same potential. Apply an electric field that is uniform at infinity and solve for the potential. Once this is done, calculate the normal component of the electric field right at the surface of the dumbbell, thus giving the charge density Σ (charge/unit area) on the dumbbell surface. The dipole moment of the dumbbell is then calculated from the average of $\Sigma\,\mathbf{r}$ over the surface and divided by the dumbbell volume.

Davis [144] gives the solution for the potential when the spheres are both held at zero potential and this solution is all that is required for solving our dumbbell problem. In calculating the polarization there are two difficult integrals that arise, which fortunately have been tabulated by Apelblat [145]. The required integrals are given by,

$$\int_{-1}^{1} \frac{P_n(x)\,dx}{(\cosh(a)-x)^{3/2}} = \frac{2^{3/2}\,e^{-(n+1/2)a}}{\sinh(a)} \tag{D.1}$$

$$\int_{-1}^{1} \frac{P_n(x)\,dx}{[\cosh(a)-x]^{5/2}} = \frac{2^{3/2}\,e^{-(n+1/2)a}[2n+1+2\coth(a)]}{3\sinh^2(a)} \tag{D.2}$$

The polarizability of the dumbbell then equals

$$\alpha_e(T)/V_p = 12(r_p-1)^3[1+2/(r_p-1)]^{3/2}Z_2 \tag{D.3}$$

$$\alpha_e(L)/V_p = 6(r_p-1)^3[1+2/(r_p-1)]^{3/2}(4S_2+4S_1+S_0) \tag{D.4}$$

$$[\sigma]_\infty = (2\alpha_e(T)/V_p + \alpha_e(L)/V_p)/3 \tag{D.5}$$

where r_p is the ratio of the center–center separation to the sphere diameter and the constants Z_2 and S_j are defined by

$$Z_2 = \sum_{n=1}^{\infty} \frac{n(n+1)}{\{\exp[(2n+1)\mu_1]+1\}} \tag{D.6}$$

$$S_j = \sum_{n=0}^{\infty} \frac{n^j}{\{\exp[(2n+1)\mu_1]-1\}} \tag{D.7}$$

where $\cosh(\mu_1) = r_p$. These infinite sums are rapidly converging so that numerical computation is straightforward. In the limit $r_p \to \infty$ only the first term of S_0 is important and we find the simple limiting behavior

$$[\sigma]_\infty \sim r_p^2, \qquad r_p \to \infty \tag{D.8}$$

The electric polarizability for two spheres without the wire [46] is quite different in general. For $r_p \to \infty$ the intrinsic conductivity $[\sigma]_\infty$ of the untethered spheres approaches 3 (the single sphere result) and for nearly touching spheres ($r_p \to 1$), $[\sigma]_\infty$ approaches $7\zeta(3)/2$ [see Eq. (3.14)].

APPENDIX E
FINITE ELEMENT METHOD COMPUTATION OF $[\eta]$ AND $[\sigma]_\infty$

Finite element methods [146] are well suited to find the extrema of *energy functionals*. In the physical cases considered in this chapter, where variational principles exist from which the relevant equations can be derived, the energy functional to be minimized is the actual energy of the system, where perhaps Lagrange multiplier terms have been added to enforce constraints. The appropriate functional for elastic problems is the elastic energy [146]

$$U(\text{elastostatic}) = \frac{1}{2}\int \varepsilon_{ij} C_{ijkl} \varepsilon_{kl} d^3r \tag{E.1}$$

where ε_{ij} is the strain tensor and C_{ijkl} is the elastic stiffness tensor and the appropriate functional for the conductivity problem [2] is the dissipated electrical power

$$U\ (\text{electrostatic}) = \frac{1}{2}\int E_i \sigma_{ij} E_j d^3r \tag{E.2}$$

where E_i is the electric field vector and σ_{ij} is the conductivity tensor.

The elastic-fluid mapping mentioned previously [17, 102, 103, 147] implies that a similar variational principle exists for the linearized fluid problem (Stokes equation), where only terms linear in the velocities are retained. This fact has been known for some time, being first discussed by Helmholz [148] and proven and elaborated on by Korteweg [149]. Millikan [150], however, proved that if one is restricted to action integrals involving only fluid velocities and first-order spatial derivatives, there will be no variational principle whose Euler equations will give the full Navier–Stokes equations.

Two recent discussions of the variational principle for viscous fluids

were given by de Veubeke [151] and Keller et al. [152], where the pressure is introduced as a Lagrange multiplier [151]:

$$\delta\left[\int \{p(\nabla\cdot u)-\frac{1}{4}\eta\theta_{ij}\theta_{ij}\right]d^3r=0 \tag{E.3}$$

$$\theta_{ij}=\frac{1}{2}\left(\frac{\partial u_j}{\partial x_i}+\frac{\partial u_i}{\partial x_j}\right) \tag{E.4}$$

$$F=-\tfrac{1}{4}\eta\theta_{ij}\theta_{ij} \tag{E.5}$$

where F is the rate of energy dissipation, $\mathbf{u}$ is the fluid velocity, and p is the pressure. Carrying out the variation indicated in Eq. (E.2) gives the linearized steady-state Navier–Stokes equation in the creeping flow limit, commonly called the Stokes equation. To enforce the incompressibility condition $\nabla\cdot\mathbf{u}=0$ requires an extra effort on the part of the would-be solver of Eq. (E.3).

In the finite element solution used in this chapter we used a formulation of the problem described by Zienkiewicz [153] in which the pressure is ignored and the incompressibility condition is only approximately maintained via a "penalty method" [146]. A term is added to the energy dissipation F of the form $\frac{1}{2}\beta(\nabla\cdot\mathbf{u})^2$, where taking a large *penalty parameter* ($\beta\to\infty$) corresponds to the incompressibile limit ($\nabla\cdot\mathbf{u}=0$). This method works extremely well, although run times become longer as the value of β is increased. Finite values of β imply some degree of compressibility of the simulated fluid.

However, it turns out that the intrinsic viscosity, or more specifically, the extra dissipated energy terms in Eq. (C.9) from Appendix C do not depend (under steady-state conditions) on the compressibility of the fluid, which means that the intrinsic viscosity does not depend on the compressibility either [154]. This allowed run times to be considerably shortened, as much smaller values of β could be used with *no change* in the final results. The argument goes as follows.

The stress tensor of a compressible isotropic fluid is a function of both the shear viscosity η and the bulk viscosity ξ [143]. The total stress tensor σ_{ij} is the sum of an ideal fluid pressure component and a viscosity component

$$\sigma_{ij}=-p\delta_{ij}+2\eta\hat{\theta}_{ij} \tag{E.6a}$$

where p is the macroscopic pressure and the viscosity contribution to the stress tensor $\hat{\theta}_{ij}$ reflects the explicit dependence on η and ξ [143],

$$\hat{\theta}_{ij} = \left(\theta_{ij} - \frac{\delta_{ij}}{3}\frac{\partial u_k}{\partial x_k}\right) + \left(\frac{\xi}{2\eta}\delta_{ij}\frac{\partial u_k}{\partial x_k}\right) \tag{E.6b}$$

For an incompressible fluid ($\nabla \cdot \mathbf{u} = 0$), the viscous stress tensor $\hat{\theta}_{ij}$ evidently reduces to θ_{ij} in Eq. (E.4). The compressibility related terms in Eq. (E.4) can be absorbed into a redefinition of the pressure P_{comp}, which then varies with the local spatial position,

$$\sigma_{ij} = -P_{\text{comp}}\delta_{ij} + 2\eta\theta_{ij} \tag{E.7a}$$

We then observe that the integral of the gradient of P_{comp} over any closed circuit C in the fluid equals zero

$$\oint_C \nabla P_{\text{comp}} \cdot d\mathbf{s} = 0 \tag{E.7b}$$

since P_{comp} is a single-valued function of position. Consequently, there is no extra dissipation [154] associated with the fluid compressibility ($\nabla \cdot \mathbf{u} \neq 0$). Notably, Eq. (E.7b) is independent of the surface boundary condition.

Finally, in actually carrying out the finite element computation for the viscosity, the "no-slip" boundary condition at a fluid–solid boundary is enforced by holding the velocity at all computational nodes either at the boundary or inside the particle fixed at zero during the conjugate gradient [25] cycles that find the minimum energy. To treat a plate geometry one simply holds the velocities of all the nodes in the appropriate planar region fixed at zero. In the analogous electrical problem one holds the voltage constant at the same nodes as for the fluid problem.

APPENDIX F
ELLIPSE TRANSPORT VIRIAL COEFFICIENTS IN $d = 2$

The intrinsic conductivity and viscosity for an ellipse in a 2D fluid can be obtained from the triaxial ellipsoid results in three dimensions by taking appropriate limits and averaging. The average required to obtain virial coefficients in $d = 2$ involves rotationally averaging around the z axis of the ellipsoid and letting a_3 (the semiaxis length in the z direction) approach infinity. We then need to evaluate A_1, A_2, and A_3 from Appendix B in the limit $a_3 \to \infty$. From Eqs. (B.1) and (B.2) along with the limit $a_3 \to \infty$ we find

$$A_1 \to 2a_2/(a_1 + a_2) \tag{F.1}$$

$$A_2 \to 2a_1/(a_1 + a_2) \tag{F.2}$$

$$A_3 \to 0 \tag{F.3}$$

and the A_i sum rule in $d = 2$ becomes,

$$A_1 + A_2 = 2 \tag{F.4}$$

The rotational average in $d = 2$ for the polarization is then

$$\langle \alpha_e \rangle = (\alpha_{11} + \alpha_{22})/2 \tag{F.5}$$

since the second-rank polarization tensor is diagonal for orthorhombic symmetry and higher. The intrinsic conductivity then equals

$$[\sigma]_\infty = (a_1 + a_2)^2/(2a_1a_2), \qquad d = 2 \tag{F.6}$$

which agrees with Garboczi et al. [155].

The intrinsic viscosity in $d = 2$ is found in the same way as the average shear modulus by rotationally averaging an elastic stiffness tensor having rectangular symmetry around the z-axis:

$$\langle G \rangle = [C_{1111} + C_{2222} + 4C_{1212} - 2C_{1122}]/8 \tag{F.7}$$

After inserting the appropriate combinations of A_1, A_2, and A_3 into Haber and Brenner's formalism given in Appendix C and [14], the rotationally averaged intrinsic viscosity becomes

$$[\eta] = \tfrac{5}{8}[Q_1 + Q_2 + 4Q_3] \tag{F.8}$$

where the Q_i values are defined in [14]. This reduces to

$$[\eta] = (a_1 + a_2)^2/(2a_1a_2) \tag{F.9}$$

which is exactly equal to the intrinsic conductivity [see Eq. (F.6)].

ACKNOWLEDGMENTS

We would like to thank Dr. Geoffrey McFadden of the Computational and Applied Mathematics laboratory at NIST for his numerical calculations of the logarithmic capacity of regions having complicated shape (Section V), Dr. Joe Hubbard for his contribution relating to understanding the role of solvent compressibility on transport properties (Appendix E), and Dr. Holly Rushmeier for generating Fig. 2.7 for us. We also thank Dr. Howard Brenner for useful discussions, encouragement, and for supplying important references.

REFERENCES

1. G. K. Batchelor, *Annu. Rev. Fluid Mech.*, **6**, 227 (1974).
2. S. Torquato, *Appl. Mech. Rev.*, **44**, 37 (1991).
3. D. J. Bergman, *Phys. Rep.*, **9**, 377 (1978).
4. (a) J. C. Maxwell, *A Treatise on Electricity and Magnetism* (Dover, N.Y., 1954), (b) J. B. Keller, *Philips Res. Rep.* **30**, 83 (1975).
5. A. S. Sangani, *Soc. Ind. Appl. Math., J. Appl. Math.*, **50**, 64 (1990).
6. H. B. Levine and D.A. McQuarrie, *J. Chem. Phys.* **49**, 4181 (1968).
7. D. J. Jeffrey, *Proc. R. Soc. London A* **335**, 355 (1973).
8. (a) H. Fricke, *Phys. Rev.* **24**, 575 (1924); (b) H. Fricke and S. Morse, *Phys. Res.*, **25**, 361 (1925).
9. (a) A. Rocha and A. Acrivos, *Q. J. Mech. Appl. Math.*, **26**, 217 (1973); (b) H.-S. Chen and A. Acrivos, *Proc. R. Soc. London A*, **349**, 261 (1976).
10. (a) A. Einstein, *Ann. Phys.* **19**, 289 (1906); **34**, 591 (1911). (b) The second-order calculation is developed by G. K. Batchelor and J. T. Green, *J. Fluid Mech.*, **56**, 401 (1972).
11. L. Onsager, *Phys. Rev.* **40**, 1028 (1932).
12. (a) N. Saito, *J. Phys. Soc. Jpn.*, **6**, 297 (1951). (b) R. Simha *J. Phys. Chem.*,**44**, 25 (1940); See Ref. 14 for a discussion of technical difficulties in this historically important calculation.
13. J. M. Rallison, *J. Fluid Mech.*, **84**, 237 (1978).
14. S. Haber and H. Brenner, *J. Coll. Int. Sci.*, **97**, 496 (1984).
15. G. I. Taylor, *Proc. R. Soc. London A*, **138**, 41 (1932).
16. (a) J. R. Lebenhaft and K. Kapral, *J. Stat. Phys.*, **20**, 25 (1979), (b) M. Fixman, *J. Phys. Chem.* **88**, 6472 (1984), (c) S. Sridharan and R. Cukier, *J. Phys. Chem.* **88**, 1237 (1984). (d) J. H. Wang, *J. Amer. Chem. Soc.*,**76**, 4755 (1954).
17. J. N. Goodier, *J. Appl. Mech. A*, **55**, 39 (1933).
18. (a) J. K. MacKenzie, *Proc. Phys. Soc. London*, **B 63**, 361 (1950); (b) J. M. Dewey, *J. Appl. Phys.*, **18**, 579 (1947); (c) J. D. Eshelby, *Proc. R. Soc. London A*, **241**, 376 (1957); (d) L. J. Walpole, *Q. J. Mech. Appl. Math.*, **25**, 153 (1972).
19. E. Guth, *J. Appl. Phys.*, **16**, 20 (1945).
20. (a) H. Froehlich and R. Sack, *Proc. R. Soc. London A*, **185**, 415 (1946), (b) R. Roscoe, *J. Fluid Mech.* **28**, 273 (1967).
21. (a) Z. Hashin, *Bull. Res. Council Isr.*, **C5**, 46 (1955), (b) Z. Hashin and S. Shtrikman, *J. Appl. Phys.*, **33**, 3125 (1962), (c) S. Praeger, *Physica*, **29**, 129 (1963); *J. Chem. Phys.*, **50**, 4305 (1969), (d) Z. Hashin, *J. Appl. Mech.*, **50**, 481 (1983).
22. (a) G. W. Milton, *J. Appl. Phys.*, **52**, 5286 (1981); *Phys. Rev. Lett.*, **46**, 542 (1981); (b) R. Lipton, *J. Mech. Phys. Solids*, **41**, 809 (1993), (c) J. D. Beasley and S. Torquato, *Phys. Fluids A*, **1**, 199 (1989).
23. E. J. Garboczi and A. R. Day, *J. Mech. Phys. Solids*, in press.
24. (a) S. Torquato and I. C. Kim, *Appl. Phys. Lett.*, **55**, 1847 (1989); (b) S. B. Lee, I. C. Kim, C. A. Miller, and S. Torquato, *Phys. Rev. B*, **39**, 11833 (1989); (c) L. M. Schwartz and J. R. Banavar, *Phys. Rev. B*, **39**, 11965 (1989); (d) K. A. Akanni, J. W. Evans, and I. S. Abramson, *Chem. Eng. Sci.*, **42**, 1945 (1987).
25. W. H. Press, B. P. Flannery, S. A. Teukolsky, and W. T. Vetterling, *Numerical Recipes*, Cambridge University Press, Cambridge, UK, 1989.

26. G. Pólya and G. Szegö, *Isoperimetric Inequalities in Mathematical Physics*, Princeton University Press, Princeton, NJ, 1951.

27. (a) J. B. Hubbard and J. F. Douglas, *Phys. Rev. E*, **47**, R-2983 (1993); (b) see [80].

28. G. Pólya, *Proc. Nat. Acad. Sci.*, **33**, 218 (1947).

29. N. S. Landkof, *Foundations of Modern Potential Theory*, Springer-Verlag, NY, 1972.

30. (a) G. Szegö, "Relation Between Different Capacity Concepts," in *Proceedings of the Conference on Differential Equations*, J. B. Diaz and L. E. Payne, Eds., University of Maryland Bookstore, College Park, MD, 1956, p. 139; (b) M. Schiffer, *Proc. Camb. Philos. Soc.* **37**, 373 (1941); (c) L. V. Ahlfors, *Conformal Invariants: Topics in Geometric Function Theory*, McGraw-Hill, NY, 1973.

31. A. Voet, *J. Phys. Chem.*, **51**, 1037 (1947).

32. (a) C. Pearce, *Br. J. Appl. Phys.*, **6**, 113 (1955); (b) R. Guillien, *Ann. Phys. (Paris)*, **16**, 205 (1941).

33. R. E. De La Rue and C. W. Tobias, *J. Electrochem. Soc.*, **106**, 827 (1959).

34. L. Sigrist and O. Dossenbach, *J. Appl. Electrochem.*, **10**, 223 (1980).

35. (a) C. R. Turner, *Chem. Engr. Sci.* **31**, 487 (1976); (b) A strong variation of thermal conductivity has been observed in metal filled plastics [D. L. Cullen, M. S. Zawojski, and A. L. Holbrook, *Plastics Engr. J.*, **44** (1), 37 (1988)]. This important example deserves quantitative examination.

36. D. A. G. Bruggeman, *Ann. Phys. (Leipzig)*, **24**, 636 (1935).

37. H.C. Brinkman, *J. Chem. Phys.*, **20**, 571 (1952).

38. (a) R. Roscoe, *Br. J. Appl. Phys.*, **3**, 267 (1952); (b) I. M. Krieger, *Adv. Coll. Int. Sci.*, **3**, 111 (1972); (c) A. B. Metzner, *J. Rheol.*, **29**, 739 (1985); (d) J. N. Goodwin and R. H. Ottewill, *Faraday Trans.*, **87**, 357 (1991).

39. G. E. Archie, *Trans. AIME*, **146**, 54 (1942).

40. P. N. Sen, C. Scala, and M. H. Cohen, *Geophysics*, **46**, 781 (1981).

41. P. D. Jackson, D. T. Smith, and P. N. Stanford, *Geophysics*, **43**, 1250 (1978).

42. (a) C. J. Bottcher, *Theory of Electric Polarization*, Elsevier, Amsterdam, 1952; (b) L.D. Landau and E. M. Lifshitz, *Electrodynamics of Continuous Media*, Pergamon, New York, 1960.

43. W. F. Brown, *J. Chem. Phys.*, **23**, 114 (1955).

44. N. Hill, W. E. Vaughn, A. H. Price, and M. Davis, *Dielectric Properties and Molecular Behavior*, Van Nostrand Reinhold, NY, 1969.

45. S. Szegö, *Duke Math. J.*, **16**, 209 (1949).

46. M. Schiffer and G. Szegö, *Trans. Am. Math. Soc.*, **67**, 130 (1949).

47. W. E. Kock, *Bell. Syst. Tech. J.*, **27**, 58 (1948).

48. G. Estrin, *J. Appl. Phys.*, **21**, 667 (1950).

49. S. Cohn, *J. Appl. Phys.*, **20**, 257 (1949); **22**, 628 (1951).

50. R. E. Collin, *Field Theory of Guided Waves*, McGraw-Hill, NY, 1960.

51. (a) P. Debye, *J. Appl. Phys.*, **15**, 338 (1944); (b) A. Peterlin, "Streaming and Stress Birefringence," in *Rheology*, Vol. 1, F. R. Eirich, Ed., Academic, New York, 1956.

52. (a) J. Stratton, *Electromagnetic Theory*, McGraw-Hill, NY, 1941; (b) G. Dassios and R. E. Kleinman, *SIAM Rev.*, **31**, 565 (1989); (c) L. Eyges, *Ann. Phys.*, **90**, 266 (1975).

53. (a) R. E. Kleinman and T. B. A. Senior, *Radio Sci.*, **7**, 937 (1972); (b) T. B. A. Senior, *Radio Sci.*, **17**, 741 (1982).

54. K. M. Siegel, *Proc. IEEE*, **51**, 232 (1962).

55. T. B. A. Senior, *Radio Sci.*, **11**, 477 (1976).

56. D. F. Herrick and T. B. A. Senior, *IEEE Trans. Ant. Prop.*, **25**, 590 (1977).

57. (a) J. B. Keller, R. E. Kleinman, and T. B. A. Senior, *J. Inst. Math. Appl.*, **9**, 14 (1972); (b) K. S. J. Lee, *Radio Sci.*, **22**, 1235 (1987).

58. W. M. Thomson (Lord Kelvin), *Reprints on Electricity and Magnetism*, MacMillan, London, 1884. See Sections 16 and 17 and Article 32, Section 633 for a discussion of the "hydrokinetic analogy" behind the M-magnetic polarizability relation.

59. A. B. Bassett, *Philos. Mag.*, **16**, 286 (1885).

60. G. Birkhoff in *Studies in Math. and Mech.: Essays in Honor of Richard Von Mises*, Academic, NY, 1954, pp. 88–96.

61. G. Birkhoff and E. H. Zarantonello, *Jets, Wakes, and Cavities*, Academic, NY, 1957, Section 6.7.

62. G. Birkhoff, *Q. Appl. Math.*, **10**, 81 (1952); **11**, 109 (1953).

63. G. Birkhoff, *Hydrodynamics: A Study of Logic, Fact, and Similitude*, Princeton University Press, Princeton, NJ, 1960, Chap. 6.

64. (a) H. Lamb, *Hydrodynamics*, Dover, NY, 1945; (b) M. Thompson, *Theoretical Hydrodynamics*, MacMillan, London, 1962.

65. G. I. Taylor, *Proc. R. Soc. A*, **120**, 13 (1928).

66. W. M. Thomson ('Lord Kelvin'), *Philos. Mag.*, **45**, 332 (1873).

67. G. I. Taylor, *Proc. R. Soc. A*, **120**, 260 (1928).

68. R. E. Kleinman and T. B. A. Senior, *IEEE Trans. Aerospace Elect. Sys.*, **11**, 672 (1975).

69. E. H. Kennard, *Irrotational Flow of Frictionless Fluids Mostly of Invariable Density*, Department of Navy Report 2299, Feb. 1967, David Taylor Model Basin, Washington, DC.

70. (a) D. M. Wrinch, *Philos. Mag.*, **48**, 1089 (1924); (b) W. G. Bickley, *Proc. London Math. Soc.*, **37**, 82 (1934).

71. (a) J. L. Taylor, *Phil. Mag.*, **9**, 160 (1930); (b) E. B. Moullin, *Proc. Phil. Soc.*, **29**, 400 (1928); (c) X. Cai and G.B. Wallis, *Phys. Fluids A*, **5**, 1614 (1993).

72. F. De Meulenaere and J. Van Bladel, *IEEE Trans. Ant. Propag.*, **25**, 198 (1977).

73. (a) E. Avras and R.F. Harrington, *IEEE Trans. Ant. Propag.*, **31**, 719 (1983); (b) N. A. McDonald, *IEEE Trans. Microwave Th. Techn.*, **35**, 20 (1987); (c) R. L. Gluckstein, R. Li, and R.K. Cooper, *IEEE Trans. Microwave Th. Techn.*, **38**, 186 (1990).

74. L. Eyges and P. Gianino, *IEEE Trans. Ant. Prop.*, **27**, 557 (1979).

75. (a) V. I. Fabrikant, *J. Phys. A*, **20**, 323 (1987); (b) V. I. Fabrikant, *J. Sound and Vibration*, **121**, 1 (1988); (c) V. I. Fabrikant, *J. Acoust. Soc.*, **80**, 1438 (1986).

76. M. Fixman, *J. Chem. Phys.*, **75**, 4040 (1981).

77. M. Schiffer, *C. R. Acad. Sci. (Paris)*, **244**, 3118 (1957).

78. (a) J. B. Keller, *J. Math. Phys.*, **5**, 548 (1964); (b) K. S. Mendelson, *J. Appl. Phys.*, **46**, 917 (1975).

79. (a) L. E. Payne and A. Weinstein, *Pacific J. Math.*, **2**, 633 (1952); (b) L. E. Payne, *Q. Appl. Math.*, **10**, 197 (1952); *Soc. Ind. Appl. Math. Rev.*, **9**, 453 (1967); (c) A. Weinstein, *Bull. Am. Math. Soc.*, **59**, 20 (1953); (d) See also [53], [55], and [57] for a review of Payne and Weinstein's results.

80. (a) H.-X. Zhou, A. Szabo, J. F. Douglas, and J. B. Hubbard, *J. Chem. Phys.*, **100**, R-3821 (1994); (b) J. F. Douglas, H.-X. Zhou, and J. B. Hubbard, *Phys. Rev. E*, **49**, 5319 (1994); (c) McKean, *J. Math. Kyoto Univ.*, **4**, 617 (1965).

81. (a) J. W. Strutt (Lord Rayleigh), *Philos. Mag.*, **44**, 28 (1897); (b) V. Twersky, *Appl. Opt.* **3**, 1150 (1964); (c) A. F. Stevenson, *J. Appl. Opt.*, **24**, 1134 (1953); (d) P. Debye, *J. Phys. Coll. Chem.*, **51**, 18 (1947); (e) J. W. Crispin and A. L. Maffett, *IEEE*, **53**, 833 (1965). See the rest of the issue for other theoretical and experimental contributions to radar (Rayleigh) scattering; (f) H. Brysk, R. E. Hiatt, V. H. Weston, and K. M. Siegel, *Can. J. Phys.*, **37**, 675 (1959).

82. (a) N. R. Labrum, *J. Appl. Phys.*, **23**, 1324 (1952); (b) W. Zhang, *IEEE Trans. Ant. Propag.*, **42**, 347 (1994).

83. J. W. Strutt (Lord Rayleigh), *Philos. Mag. Ser.*, 4 **41**, 447 (1871); *Ser. 6* **35**, 373 (1918); *Proc. London Math. Soc.*, **4**, 253 (1872).

84. J. Van Bladel, *J. Acoust. Soc. Am.*, **44**, 1069 (1968).

85. T. B. A. Senior, *J. Acoust. Soc. Am.*, **53**, 742 (1973).

86. D. S. Jones, *Proc. R. Soc. Edin. A*, **83**, 245 (1979).

87. J. W. Strutt (Lord Rayleigh), *Philos. Mag.*, **43**, 259 (1897); see also [82a].

88. (a) H. A. Bethe, *Phys. Rev.*, **66**, 163 (1944); (b) H. A. Bethe, "Lumped Constants for Small Irises," M. I. T. Radiation Laboratory Reports. 43–22 (1943); (c) H. Levine and J. Schwinger, *Phys. Rev.*, **74**, 958 (1948); *Comm. Pure Appl. Math.*, **3**, 355 (1950); (d) D. L. Jaggard and C. H. Papas, *Appl. Phys.*, **15**, 21 (1978); (e) T. Wang, J. R. Mautz, and R. F. Harrington, *Radio Sci.*, **22**, 1289 (1979).

89. C. J. Bouwkamp, *Rep. Prog. Phys.*, **17**, 35 (1954).

90. J. Van Bladel, *Proc. IEEE*, **17**, 1098 (1970).

91. J. Van Bladel, *Radio Sci.*, **14**, 319 (1979).

92. (a) T. B. A. Senior and D. J. Ahlgren, *IEEE Trans. Ant. Propag.*, **21**, 134 (1973); (b) T. B. A. Senior and T. M. Willis III, *IEEE Trans. Ant. Propag.*, **30**, 1271 (1982).

93. (a) R. L. Hamilton and O. K. Crosser, *I.E.C. Fundamentals*, **1**, 187 (1962); (b) J. Francl and W. D. Kingery, *J. Am. Ceram. Soc.*, **37**, 99 (1954).

94. K. S. Mendelson and H. H. Cohen, *Geophysics*, **47**, 257 (1982). See also [42].

95. (a) T. Murai, *Prog. Theor. Phys.*, **27**, 899 (1962); (b) G. Araki and T. Murai, *Prog. Theor. Phys.*, **8**, 639 (1952); (c) H. Kuhn, *J. Chem. Phys.*, **17**, 1198 (1949).

96. H. Sternlicht, *J. Chem. Phys.*, **40**, 1175 (1964).

97. (a) V. Belovitch and J. Boersma, *Philips J. Res.*, **38**, 79 (1983); (b) T. Miloh, G. Waisman, and D. Weihs, *J. Engr. Math.*, **12**, 1 (1978). This work calculates the magnetic polarizability (added or virtual mass) of tori. The intrinsic conductivity $[\sigma]_0$ of insulating toroidal particles is never greater than 12% of the spherical particle value or less than the spherical particle value so that $[\sigma]_0$ is rather insensitive to shape.

98. M. Fixman, *J. Chem Phys.*, **76**, 6124 (1982).

99. (a) K. F. Freed and S. F. Edwards, *J. Chem. Phys.*, **62**, 4032 (1975); (b) G. J. Kynch, *Br. J. Phys.*, **3**, S-5 (1954); *Proc. R. Soc. London A*, **237**, 90 (1956).

100. T. F. Ford, *J. Phys. Chem.*, **64**, 1168 (1960). This work references and discusses Bancelin's data and the interchange between Einstein and Bancelin, and is more accessible than Bancelin's original paper.
101. (a) D. J. Jeffrey and A. Acrivos, *A.I. Chem. E.*, **22**, 417 (1976); (b) R. Rutgers, *Rheol. Acta*, **2**, 305 (1964).
102. J. W. Strutt (Lord Rayleigh), *Theory of Sound, Vol. 2* (Dover, N.Y., 1945).
103. R. Hill and G. Power, *Q. J. Mech. and Appl. Math.*, **9**, 313 (1956).
104. (a) J. S. Chang, E. B. Christiansen, and A. D. Baer, *J. Appl. Polym. Sci.*, **15**, 2007 (1971); (b) N.J. Mills, *J. Appl. Polym. Sci.*, **15**, 2791 (1971).
105. W. N. Bond, *Philos. Mag.*, **4**, 889 (1927); **5**, 794 (1928).
106. C. Brenner, *Can. J. Chem. Engr.*, **53**, 126 (1975).
107. J. W. Mehl, J. L. Oncley, and R. Simha, *Nature* (London), **92**, 132 (1940).
108. J. Kirkwood and J. Riseman, *J. Chem. Phys.*, **16**, 565 (1948).
109. P. Debye and A. M. Bueche, *J. Chem. Phys.*, **16**, 573 (1948).
110. S. Kim and S.-Y. Lu., *Int. J. Multiphase Flow*, **10**, 113 (1984).
111. G. K. Batchelor, *J. Fluid Mech.*, **41**, 545 (1970). See Eq. (5.11) of this work.
112. E. J. Hinch, *J. Fluid Mech.*, **54**, 423 (1972).
113. J. F. Brady, *Int. J. Multiphase Flow*, **10**, 113 (1984).
114. G. Bossis, A. Meunier, and J. F. Brady, *J. Chem. Phys.*, **94**, 5064 (1991). The results of this work suggest to us that $[\eta]$ of flocculated aggregates, held together by tenuous forces, should be approximately proportional to $[\sigma]_0$, rather than $[\sigma]_\infty$. This possibility deserves further consideration.
115. R. P. Kanwal, *J. Fluid Mech.*, **10**, 17 (1960).
116. J. Riseman and J. G. Kirkwood, *J. Chem. Phys.*, **17**, 442 (1949).
117. H. Brenner, *Int. J. Multiphase Flow*, **1**, 195 (1974).
118. S. Wakiya, *J. Phys. Soc. Jpn.*, **31**, 1581 (1972).
119. G. de la Torre and V. Bloomfield, *Q. Rev. Biophys.*, **14**, 81 (1981).
120. (a) H. A. Scheraga, *J. Chem. Phys.*, **23**, 1526 (1955); (b) R. Simha, *J. Res. N.B.S.*, **42**, 409 (1949); (c) J. W. Miles, *J. Appl. Phys.*, **38**, 192 (1967).
121. (a) M. Zuzovsky and H. Brenner, *J. Appl. Math. Phys.*, **28**, 979 (1977). See especially Eq. (77); (b) K. C. Nunan and J. B. Keller, *J. Fluid Mech.*, **142**, 269 (1984); (c) M. Zuzovsky, P.M. Adler, and H. Brenner, *Phys. Fluids* **26**, 1714 (1983).
122. (a) T. T. Taylor, *J. Res. NBS* **64**, 135 (1960); (b) P. K. Wang, *IEEE Trans. Ant. Prop.*, **32**, 956 (1984); (c) M. Fixman, *J. Chem. Phys.*, **75**, 4040 (1981).
123. B. B. Mandelbrot, *The Fractal Geometry of Nature*, W. H. Freeman and Co., San Francisco, CA, 1982.
124. M. Belzons, R. Blanc, and C. Carmoin, *C. R. Acad. Sci. (Paris)*, **292**, 68 (1981).
125. F. Bauer, P. Garabedian, D. Korn, and A. Jameson, *Lect. Notes Econ. Math. Sys.*, **108**, 1975.
126. G. B. McFadden, P. W. Voorhees, R. F. Boisvert, and D. I. Meiron, *J. Sci. Comp. 1*, **117** (1986). The methods of [125] and [126] were adapted to the calculation of the logarithmic capacity by G. B. McFadden of the Computational and Applied Mathmatics Laboratory at NIST.
127. (a) M. F. Thorpe, *Proc. R. Soc. London A*, **437**, 215 (1992); (b) J. H. Hetherington and M. F. Thorpe, *Proc. R. Soc. London A*, **438**, 591 (1992).
128. G. Pólya and G. Szegö, *Am. J. Math.*, **68**, 1 (1945).

129. O. D. Kellogg, *Foundations of Potential Theory*, (Springer-Verlag, Berlin, 1929, see p. 331.

130. (a) A. Dvoretsky, P. Erdös, and S. Kakutani, *Acta Sci. Math. (Szeged)* **12**, 75 (1950); (b) S. J. Taylor, *Proc. Camp. Phil. Soc.*, **51**, 265 (1955).

131. H. Hasimoto, *J. Phys. Soc. Jpn.*, **13**, 633 (1958).

132. (a) S. Cohn, *Proc. I.R.E.*, **39**, 1416 (1951); (b) S. Cohn, *Proc. I.R.E.*, **40**, 1069 (1952).

133. (a) R. J. S. Brown, *Geophysics*, **45**, 1269 (1980); (b) M. A. Biot, *J. Acoust. Soc. Am.*, **28**, 168 (1956).

134. D. L. Johnson and P. N. Sen, *Phys. Rev. B*, **24**, 2486 (1981).

135. J. W. Strutt (Lord Rayleigh), *Philos. Mag.*, **4**, 481 (1892).

136. D. L. Johnson, T. J. Plona, C. Scala, F. Pasierb, and H. Kojima, *Phys. Rev. Lett.*, **49**, 1840 (1982).

137. J. G. Berryman, *Phys. Rev. B*, **27**, 7789 (1983).

138. A. Atkinson and A. K. Nickerson, *J. Mat. Sci.*, **19**, 3068 (1984).

139. J. F. Nye, *Physical properties of crystals: Their representation by tensors and matrices*, Oxford University Press, London, 1957.

140. G. Arfken, *Mathematical Methods for Physicists*, Academic, New York, 1970, p. 121.

141. J. P. Watt, *J. Appl. Phys.*, **51**, 1525 (1980).

142. L. D. Landau and E. M. Lifshitz, *Theory of Elasticity*, Pergamon Press, New York, 1970.

143. L. D. Landau and E. M. Lifshitz, *Fluid Mechanics*, Pergamon Press, New York, 1959.

144. M. H. Davis, *Q. J. Mech. Appl. Math.*, **17**, 499 (1964).

145. A. Apelblat, *Physical Sciences Data*, Vol. 13, Elsevier, Amsterdam, 1983, p. 56.

146. R. D. Cook, D. S. Malkus, and M. E. Plesha, *Concepts and Applications of Finite Element Analysis*, Wiley, New York, 1989.

147. R. M. Christensen, *Mechanics of Composite Materials*, Krieger Publishing Co., Malabar, FL, 1991.

148. H. Helmholz, *Wiss. Abh.*, **1**, 223. See also the collected works of Helmholz.

149. D. J. Korteweg, *Philos. Mag.*, **16**, 112 (1883).

150. C.B. Millikan, *Philos. Mag.*, **7**, 641 (1929).

151. B. Fraeijs de Veubeke, "Variational principles in fluid mechanics and finite element applications," in *Progress in Numerical Fluid Dynamics Lecture Notes in Physics*, J. Ehlers, K. Hepp, H. A. Weidenmuller, and J. Zittartz, Eds., Springer-Verlag, Heidelberg, 1975. Vol. 41, pp 226–259

152. (a) J. B. Keller, L.A. Rubenfeld, and J.E. Molyneux, *J. Fluid Mech.*, **30**, 97 (1967); (b) R. Skalak, *J. Fluid Mech.*, **42**, 527 (1951).

153. O. C. Zienkiewicz, "Viscous, incompressible flow with special reference to non-Newtonian (plastic) fluids," in *Finite Elements in Fluids—Volume I: Viscous Flow and Hydrodynamics*, R. H. Gallagher, J. T. Oden, C. Taylor, and O. C. Zienkiewicz, Eds., Wiley, London, 1975, pp. 25–56.

154. P. J. Stiles and J. B. Hubbard, *Chem. Phys. Lett.*, **105**, 655 (1984).

155. E. J. Garboczi, M. F. Thorpe, M. S. DeVries, and A. R. Day, *Phys. Rev. A*, **43**, 6473 (1991).